Fracture Prediction for Square Hollow Section Braces under Extremely Low Cycle Fatigue

Fei Xu[1], Wen-Hao Pan[3], Tak-Ming Chan[2]*, Therese Sheehan[4], Leroy Gardner[5]

1. School of Civil Engineering Chongqing University, and Key Laboratory of New Technology for Construction of Cities in Mountain Area (Chongqing University), Ministry of Education, Chongqing, China
2. Department of Civil and Environmental Engineering, The Hong Kong Polytechnic University, Hong Kong
3. College of Civil Engineering and Architecture, Zhejiang University, China
4. Faculty of Engineering and Informatics, University of Bradford, United Kingdom;
5. Department of Civil and Environmental Engineering, Imperial College London, South Kensington Campus, United Kingdom.

Abstract: This paper examines the extremely low cycle fatigue (ELCF) fracture of concentrically loaded square hollow section (SHS) braces subjected to cyclic loading. Numerical analyses are presented for both individual bracing members and bracing members integrated into concentrically braced frames (CBFs). The behaviour of the individual members was predicted using solid finite element (FE) simulations that employed a ductile fracture model and a nonlinear damage evolution rule. The solid FE model, which was validated using data from experiments, could adequately predict both the hysteretic response and the ELCF fracture cracking process. The coupled effects of instabilities (i.e. local and global buckling) and fracture on the ELCF performance of the braces were assessed, and the rotation capacity prior to fracture was quantified. This quantified rotation capacity was then incorporated into fibre-based FE models of CBFs as a member-level fracture criterion. The structure-level simulations were able to accurately capture the complex interactions between the frame components, i.e. the columns, beams, brace-gusset-plate connections and beam-to-column connections, and hence replicate the overall behaviour of CBFs, specifically, two-storey chevron braced frames. The influence of cross-section and member slenderness was evaluated and the importance of considering both in the development of cross-section slenderness limits was highlighted. The combined member- and structure-level simulation approach is proposed as an accurate and efficient means of assessing the seismic performance of CBFs.

Keywords: Braces; Square hollow sections; Extremely low cycle fatigue; Fracture prediction; Numerical study; Concentrically braced frames; Fibre-based finite element model; Seismic; Earthquake resistance

*Corresponding author: tak-ming.chan@polyu.edu.hk

1. Introduction

Concentrically braced frames (CBFs) are a widely used form of earthquake-resisting structure because of their high structural efficiency and the ability of the diagonal bracing members to dissipate energy. Hollow structural sections (HSSs) are becoming increasingly prevalent as bracing members because of their structural performance and visual appeal. However, experimental studies (i.e. Tremblay [1], Nip *et al.* [2], Fell [3], Shaback and Brown [4], Goggins *et al.* [5], Elchalakani *et al.* [6] and Sheehan and Chan [7]) have shown that the energy-dissipation performance of the HSS braces is often compromised by the combined effects of buckling and fracture at the mid-length.

Square hollow section (SHS) braces are more vulnerable to localised deformation-induced fracture than their circular hollow section (CHS) counterparts. The fracture crack usually initiates at the corners of SHS braces followed by the propagation of the cracking transversely across one flange face [2]. Finally, the crack develops through the entire section when the brace is loaded in tension, leading to a sudden loss of strength and functional failure. As a result, the pre-set ductility levels, such as the maximum inter-storey drift for a braced frame, may fail to be achieved due to the premature fracture. In previous experimental investigations [1-7], the cross-sectional slenderness (width-to-thickness ratio) and member slenderness were found to have a major influence on the cyclic-loading-induced fracture of bracing members. For SHS braces to achieve adequate ductility and survive large, repeated post-buckling deformations before fracture, their cross-sections need to meet the strict width-to-thickness (B/t) ratio limits. These limits are $B/t \le 0.76\sqrt{E/\left(R_y f_y\right)}$ for ordinary concentrically braced frames (OCBFs) and $B/t \le 0.65\sqrt{E/\left(R_y f_y\right)}$ for special concentrically brace frames (SCBFs), as stipulated in the seismic design specification AISC 341-16 [8], where E and f_y are the elastic modulus and yield strength of steel respectively and R_y is the ratio of the expected yield strength to the specified minimum yield strength, as given in AISC 360-16 [8]. In addition, to obtain satisfactory post-buckling energy dissipation, the member

slenderness limits in AISC 341-16 [8] are stipulated as $L_c / r \leq 4\sqrt{E / f_y}$ for OCBFs and 200 for SCBFs, where L_c is the effective length of the brace. These limits on the cross-sectional and member slenderness values are uncoupled in AISC 341-16 [8], but experimental results [2,7] have indicated that there is, in fact, a combined effect of cross-sectional and member slenderness on fracture life. Quantifying this coupled effect on the fracture life of bracing members remains a challenge. The manufacturing process has also been reported to have a marked influence on the ductility and fracture life of both SHS and CHS braces in tests [2,7,9]. Hot-finished tubular sections have essentially homogeneous material properties, a sharply defined yield point and very low levels of residual stress. Cold-formed tubular sections, on the other hand, owing to the cold work experienced during section forming, exhibit a more rounded stress-strain response exacerbated by high bending residual stresses, reduced ductility, and in the case of SHS, enhanced corner strength [2, 10]. While cyclic testing of cold -formed steel tubular braces has been carried out, there have been no experimental studies that have directly examined the influence of the dominant bending residual stress as on the processes of fracture initiation and propagation [10]. While cyclic testing of cold-formed steel tubular braces has been carried out, there have been no experimental studies that have directly examined the influence of the dominant bending residual stresses on the process of fracture initiation and propagation [11].

In seismic design, several interrelated parameters have an impact on the fracture life of braces and a quantitative understanding of the effects of these parameters would enable more informed member selection. The high cost of a comprehensive full-scale brace testing programme necessitates the development of an advanced numerical simulation study. This advanced numerical simulation method should adequately capture the entire response of the extremely low cycle fatigue (ELCF) induced fracture process, including crack initiation and propagation, and could offer an efficient and cost-effective alternative to laboratory testing. Different fracture prediction methodologies have been developed for use in parallel with numerical simulations to predict ELCF fracture at the member-level, including: (1) the cycle

87 counting technique applied through fibre-based elements [12], (2) post-processing of FE
88 simulation data [2] using the "rain flow" counting technique in conjunction with the Coffin-
89 Mason strain-life relationship [13,14] and (3) finite element (FE) simulations with a fracture
90 criterion [3,15,16]. The first approach is frequently employed in structure-level simulations, i.e.
91 braced frames, owing to the computational efficiency of fibre-based elements, while the second
92 and third approaches are commonly used for more refined member-level modelling. Among
93 these three approaches, the third approach can generally achieve the most accurate results
94 through explicit modelling of the fracture development process.

95 Kanvinde and Deierlein [17] proposed a physics-based prediction model named the cyclic
96 void growth model (CVGM) based on the micro-mechanism of void growth and coalescence
97 [18,19]. The CVGM model assumes that ELCF fracture depends on stress triaxiality (η) and
98 inherent damage accumulation due to cyclic loading, following observations of similar dimple-
99 dominated fracture profiles under both monotonic and ELCF loading. Recently the Lode angle
100 (θ), which captures the effects of deviatoric stress states, was found to have a significant
101 influence on metal ductile fracture at low stress triaxiality levels ($\eta < 0.5$) [20-23]. Therefore,
102 ductile fracture models that feature both stress triaxiality and Lode angle, incorporating a
103 nonlinear damage accumulation rule, have subsequently been proposed by researchers [24-29].
104 These models are based on and verified against material (coupon)-level tests.

105 In this study, a material-level fracture model with a damage accumulation rule that can
106 capture the dependence on both stress triaxiality and Lode angle is adopted into the simulation
107 model of individual tubular braces. The influence of the manufacturing process on the material
108 properties is considered in the simulations by adopting the material stress-strain characteristics
109 obtained from tests on coupons cut from the flat and corner regions of reference tubes. In the
110 case of the cold-formed members, the influence of the bending residual stresses is directly
111 captured in the stress-strain curves, while the enhanced yield strength and reduced ductility in
112 the corner regions is accounted for by assigning different material properties to the different
113 portions of the modelled cross-sections [10, 30-33]. The applicability, accuracy and efficiency

of the material-level fracture model in predicting the extremely low cycle fatigue (ELCF) fracture of cyclically loaded bracing members (at member-level) are evaluated. The established FE models are validated against available results sourced from different test programmes and are used to conduct a parametric study to extend the test database. The coupled effects of the instabilities (i.e. local and global) and fracture on the deformation capacity of the braces are assessed and quantified with respect to the member geometry, material properties and manufacturing process. A brace fracture life prediction equation is proposed in terms of the global rotation prior to fracture; this is employed in structure-level simulations of CBFs using a fibre-based finite element model. The combined member- and structure-level simulation approach is proposed as an accurate and efficient means of assessing the seismic performance of CBFs. Based on both member-level and structure-level simulations, the seismic performance of CBFs is assessed against the requirements of AISC 341-16 [8].

2. Numerical Investigation of Braces

2.1. FE modelling methodology

Finite element models were established using ABAQUS/Standard [34] to perform the quasi-static simulation of bracing members under ELCF loading conditions [35], capturing the hysteretic response, fracture initiation and propagation. The test specimens and loading protocols from two programmes [2,3] are used for the model validation. The geometric information and loading protocols are summarised and presented in Fig. 1 and Table 1. Utilising symmetry, only one-quarter of the bracing members was modelled, as shown in Fig. 2. The axial load was applied under displacement control to the reference point RP-2, to which all degrees of freedom on the end surface were coupled. The same displacement histories as those employed in the test programmes [2,3] were applied in the validation models. The Type A displacement history [2], as shown in Fig. 1(c), which follows the European Convention for Constructional Steelwork (ECCS) loading protocol [35] with each cycle beginning with tensile force, was adopted in the parametric investigation; this was used in favour of the Type B and

C loading protocols since these represent specific ground motions, i.e., far-field ground motions (Type B) and near-fault ground motions (Type C).

Three-dimensional C3D8R solid elements [36] were adopted in the FE models. Another set of FE models were constructed with three-dimensional S4R shell elements for comparison. Shell element-based models offer the advantage of simulating the buckling and post-buckling performance of tubular structures with relatively low computational time and a competitive degree of accuracy compared with solid-element based models. Typical comparisons between the solid and shell FE models of the full hysteretic responses and the key points during the fracture process, i.e. fracture initiation and complete rupture, are presented, together with the corresponding experimental results [2] in Fig. 3. The FE models constructed using the solid elements could simulate the whole cracking process, including initiation and propagation through the thickness and cross-section, while the shell element-based models failed to capture the cracking throughout the thickness. Hence, although the predictions of fracture throughout the cross-section of the two FE models occurred within the same cycle and the obtained tensile capacities were similar, the C3D8R-element based models were favoured for the remainder of this study owing to their ability to accurately capture the full fracture process.

A refined mesh was used in the region of the mid-length and at the ends of the models, where local buckling was anticipated to occur. The lengths of the refined regions are presented in Fig. 2. A mesh sensitivity and convergence study was conducted using element sizes of 1 mm, 1.5 mm and 2.5 mm for the refined region along both the longitudinal axis and the circumferential direction, and an element size of 15 mm for the coarse mesh region. The number of elements through the thickness was set as the larger value of 3 and $t/1.5$. It was found that the coarse mesh would postpone the occurrence of fracture initiation in the tube-wall, but there was only a minor effect on the complete fracture of the SHS bracing members, as presented in Fig. 4. Considering the computational time, an element size of 1.5 mm was adopted in the refined regions of the subsequent FE analyses. The total number of elements in the FE model of specimen 40×40×3×1250-CS-HR was approximately 52,500. The adopted

mesh for a typical FE model is presented in Fig. 2.

Initial geometric imperfections, both global and local, were introduced in the FE models by the superposition of eigenmodes. A sensitivity study was conducted to access the influence of the initial imperfections on buckling and fracture. The amplitudes of the global and local imperfections were varied from $L/500$ to $L/5000$ and $t/50$ to $t/500$, respectively. Global buckling occurred at an earlier stage in the models with larger imperfection amplitudes, as expected, while the occurrence of fracture initiation differed by only one cycle for the investigated ranges of imperfection amplitudes. Comparisons were made between the number of cycles to global buckling, local buckling and fracture by minimizing the sum of the squares of the differences between the numerical and experimental results. From these comparisons, the optimum imperfection amplitudes for each test programme were determined, as listed in Table 2. A global imperfection value of $L/1500$ and local imperfection values of $t/200$ and $t/150$ for hot-rolled (HR) and cold-formed (CF) members, respectively, were used in the parametric studies.

2.2. Plasticity and fracture models

2.2.1 Plasticity modelling

The adopted constitutive model was based on the work of Lemaitre and Chaboche [37] and featured the von Mises yield criterion and a combined isotropic/kinematic hardening rule. The evolution of the kinematic hardening component of the model is described by Eq. (1).

$$\alpha = \sum_{k=1}^{n} \alpha_{\mathrm{k}} \tag{1a}$$

$$d\alpha_{\mathrm{k}} = C_{\mathrm{k}} \frac{1}{\sigma_0} (\sigma - \alpha) d\bar{\varepsilon}^{pl} - \gamma_{\mathrm{k}} \alpha_{\mathrm{k}} d\bar{\varepsilon}^{pl} \tag{1b}$$

where n is the total number of backstress components, α is the overall back stress, σ_{k} is the k^{th} backstress, $\bar{\varepsilon}^{pl}$ is the equivalent plastic strain, C_{k} is the k^{th} initial kinematic hardening modulus, γ_{k} is the k^{th} rate of decrease of C_{k} and σ_0 is the size of the yield surface defined by the isotropic

191 hardening equation, given by Eq. (2). In this study, multi backstress components were adopted
192 in the calibration process to accurately capture the kinematic hardening of the steels.

193 $$\sigma_0 = \sigma\big|_0 + Q_\infty\left(1 - e^{-b\,\bar{\varepsilon}^{\mathrm{pl}}}\right) \quad (2)$$

194 where $\sigma\big|_0$ is the yield stress at zero plastic strain, Q_∞ is the maximum change in size of the
195 yield surface and *b* is the rate of change of the yield surface size with increasing plastic strain.
196 The strength enhancement in the corner regions [38] of the studied cold-formed SHS
197 braces was considered by applying measured corner material properties [2,3] to the curved
198 corner portions of the FE models, plus an extension into the flat regions on either side equal to
199 the section thickness. The model parameters of the combined isotropic/kinematic hardening
200 rule were calibrated according to the ABAQUS documentation [36] for each test programme,
201 as listed in Table 3.
202 2.2.2 Fracture modelling
203 A continuum damage mechanics approach [37], implemented in ABAQUS [34], was used in
204 this research to describe the progressive degradation of the material under cyclic loading. A
205 typical uniaxial stress-strain curve with progressive damage degradation is shown in Fig. 5
206 (solid curve *a*-*b*-*c*-*d*). The curve *a*-*b*-*c*-*d*' represents the behaviour of the material without
207 considering damage. Point c marks the onset of damage, taken as the point of fracture initiation.
208 Beyond this point, the material response degrades under the principle of strain-equivalence. In
209 the developed finite element simulations, Point *c* was determined using a fracture initiation
210 criterion and the material softening behaviour was described using a damage evolution rule.
211 The ductile fracture of metals has been recognized as being dependent on stress triaxiality
212 (η) and Lode angle (θ). The modified Mohr-Coulomb (MMC) model [39] is a
213 phenomenological ductile fracture prediction model, proposed and validated at the material-
214 level (coupon); this model has been adopted in FE simulations at member-level [40-43] and
215 shown to be capable of predicting fracture initiation and propagation. The MMC fracture model

in the space of ($\bar{\varepsilon}_f$, η , $\bar{\theta}$), used in conjunction with the von Mises yielding function, is expressed in Eq. (3), with the corresponding cut-off region described in Eq. (4).

$$\bar{\varepsilon}_f = \left\{ \frac{A}{c_2} \left[\sqrt{\frac{1+c_1^2}{3}} \cos\left(\frac{\bar{\theta}\pi}{6} \right) + c_1 \left(\eta + \frac{1}{3} \sin\left(\frac{\bar{\theta}\pi}{6} \right) \right) \right] \right\}^{-\frac{1}{n}} \tag{3}$$

$$\sqrt{\frac{1+c_1^2}{3}} \cos\left(\frac{\bar{\theta}\pi}{6} \right) + c_1 \left(\eta + \frac{1}{3} \sin\left(\frac{\bar{\theta}\pi}{6} \right) \right) \leq 0 \tag{4}$$

where $\bar{\varepsilon}_f$ is the equivalent fracture strain, η is the stress triaxiality defined by Eq. (5), $\bar{\theta}$ = (1-$6\theta/\pi$) is the normalised Lode angle, θ is the Lode angle defined by Eq. (6), A and n are the material strain-hardening parameters that can be calibrated from the true stress-strain curve by fitting Hollomon's [44] or Swift's [45] power laws and c_1 and c_2 are the friction coefficient and the maximum shear strength in the Mohr-Coulomb criterion, respectively.

$$\eta = \frac{\sigma_m}{\bar{\sigma}} \tag{5}$$

$$\theta = \frac{1}{3} \arccos(\xi) = \frac{1}{3} \arccos\left(\frac{27}{2} \frac{J_3}{\bar{\sigma}^3} \right) \tag{6}$$

$$\bar{\sigma} = \sqrt{3J_2} \tag{7}$$

where $\bar{\sigma}$ is the von Mises stress, σ_m is the mean stress, ξ is the normalised third deviatoric stress invariant and J_2 and J_3 are the second and third deviatoric stress invariants, respectively.

The calibrated parameters of the MMC model for each test programme are listed in Table 4. The parameters A and n, representing the flow strength parameters of the material, can be derived from the results of conventional tensile coupon tests. Typically, the parameters c_1 and c_2 are calibrated based on tests on notched round bars with different notched radii for the high stress triaxiality domain and flat coupons (dog-bone, central hole and butterfly types and circular punch disk specimens) for the intermediate and low stress triaxiality domains. The parameters can be determined by minimizing the differences in average equivalent plastic strain between the test and simulation results at the onset of fracture. With limited material test

data available, a simplified MMC model calibration procedure was proposed in [40-41], utilising conventional tensile coupon test results only. In the simplified procedure, in addition to the parameters A and n, the material parameter c_2, accounting for the shear strength of the material [46] can also be estimated from conventional coupon tests [47]. Meanwhile, c_1 can be assumed to be constant for material with similar crystallographic structures. A sensitivity study was conducted in [40] to assess the effect of the parameter c_1 on the prediction of fracture initiation. It was found that a value of 0.12 is applicable for structural steels with nominal yield strengths ranging from 235 MPa to 345 MPa. Further details on the calibration of the model parameters are provided by Xu et al. [40].

The linear damage accumulation rule has been found to adequately predict material fracture initiation under monotonic loading [39, 48]. However, for the non-monotonic loading cases, both load history and nonlinear damage evolution should be considered [17,25-28]. Two weighting functions [26] were therefore adopted in this study relating to nonlinear accumulation (in Eq. (8)) and the load history effect (in Eq. (9)).

$$F_D\left(D_{\mathrm{FI}}\right)=\left(c_{\mathrm{g}}D_{\mathrm{FI}}+\frac{c_{\mathrm{g}}}{e^{c_{\mathrm{g}}}-1}\right) \tag{8}$$

$$F_{\mathrm{H}}\left(D_{\mathrm{FI}},\mu_{\mathrm{h}}\right)=\left(1+c_{\mathrm{h}}\cdot D_{\mathrm{FI}}^{\beta_1}\cdot\mu_{\mathrm{h}}^{\beta_2}\right)^{k_{\mathrm{h}}} \tag{9}$$

where c_{g} is the parameter of the extension function for the nonlinear damage rule, c_{h}, β_1, β_2 and k_{h} are the parameters of the extension function for load-change effects and μ_{h} is associated with the backstress and current stress tensors to capture the reverse loading effects, as defined by

$$\mu_{\mathrm{h}}=\int_0^{\bar{\varepsilon}^{pl}}\left(1-\frac{\sigma_{ij}:\alpha_{ij}}{\left\|\sigma_{ij}\right\|\cdot\left\|\alpha_{ij}\right\|}\right)d\bar{\varepsilon}^{pl} \tag{10}$$

The hybrid damage evolution rule employed is presented in an incremental form as

$$dD_{\mathrm{FI}}=F_{\mathrm{D}}\,F_{\mathrm{H}}\frac{d\bar{\varepsilon}^{pl}}{\bar{\varepsilon}_f(\eta,\bar{\theta})} \tag{11}$$

where dD_{FI} is the damage increment, $\bar{\varepsilon}^{pl}$ is the equivalent plastic strain, as defined by Eq. (12), $d\bar{\varepsilon}^{pl}$ is the equivalent plastic strain rate, and α and σ are the backstress and current stress tensors, respectively.

$$\bar{\varepsilon}^{pl} = \int_0^t \sqrt{\frac{2}{3} d\varepsilon^{pl} : d\varepsilon^{pl}}\, dt \tag{12}$$

The range of the damage indicator D_{FI} is assumed to be [0,1.0]. D_{FI} = 0 represents the material behaviour before the plastic stage, while D_{FI} = 1.0 denotes the initiation of fracture. It is assumed that, in the initial state, the material is free from accumulated plastic strains or localised damage caused by manufacturing and shipping. A group of consistent values of c_g, c_h, β_1, β_2 and k_h has been determined from minimizing the average errors of the number of cycles to fracture between the experimental and numerical results, as listed in Table 4. Figs. 6(a) and 6(b) present the evolution of the accumulation damage indicator D_{FI} of test specimen 40×40×3×1250-CS-HR, reported in [2], with the stress triaxiality and normalised Lode angle under cyclic loading respectively. Brace fracture can be seen to be triggered by the amplified strain accumulated at the corner region, as the damage indicator increases significantly after the occurrence of local buckling.

The post-initiation softening rule is described by a linear relationship between the material degradation and the equivalent plastic strain, as shown in Eqs. (13)-(15). This can help to simulate fracture propagation and the correct cracking modes [17, 48, 49] and achieve better convergence without a sudden degradation of stress. The softening rule is defined as a function of the effective plastic displacement, which is a simulation technique to alleviate mesh dependence [36], as shown in Eq. (15).

$$\tilde{E} = E\,(1\text{-}D_{post}) \tag{13}$$

$$\tilde{\boldsymbol{\sigma}} = \boldsymbol{\sigma}/\,(1\text{-}D_{post}) \tag{14}$$

where $\tilde{E}$ is the elastic modulus of the damaged material, E is the elastic modulus of the undamaged material, $\tilde{\boldsymbol{\sigma}}$ is the effective stress tensor, $\boldsymbol{\sigma}$ is the usual stress tensor and D_{post} is the damage variable.

$$dD_{\text{post}} = \frac{L_C d\bar{\varepsilon}^{pl}}{\bar{u}_f^{pl}} \quad (15)$$

where L_C is the characteristic length of the element for a specified FE model, which, for the adopted solid elements, is determined as the cube root of the integration point volume [36].

A flow chart of the fracture simulation process is presented in Fig. 7. A USDFLD subroutine was adopted to facilitate the fracture prediction when using the MMC model. The element was set to fail at the maximum post initiation degradation with a residual stiffness of 2% to avoid severe non-symmetry of the Jacobian matrix and convergence problems.

2.3. Validation

Two test programmes [2,3] focusing on the cyclic behaviour of the individual bracing members, were adopted to validate the developed FE models. The number of cycles to buckling, general hysteretic response and fracture process, including initiation and propagation, were compared between the tests and numerical calculations. The comparisons demonstrate that the proposed FE model can accurately predict local buckling-induced ductile fracture under ELCF loading.

The comparisons of the full hysteretic curves between the experimental and numerical results are shown in Figs. 8 and 9. The key stages of the fracture development, i.e. crack initiation, corner opening and complete fracture, are also presented and compared between the test (if reported) and simulation results in Figs. 8 and 9. Good agreement can be seen from the comparisons. To reaffirm the significance of simulating fracture of bracing members in understanding their performance, results from an FE model without fracture modelling were also obtained. The comparison, as presented in Fig. 3, indicates that the brace deformation capacity and post fracture behaviour can be overestimated in the absence of the fracture criterion.

Table 2 summarises the comparisons of the numbers of cycles to global buckling, local buckling and fracture. The definitions of the typical stages of ELCF fracture are illustrated in Fig. 10. Generally, the results indicate that the simulation was reasonably accurate. It should

311 be noted that the convergence problems often arise in the post-fracture stage due to the material
312 softening and stiffness degradation beyond fracture in implicit analysis programmes [36].
313 The ELCF fracture failure mode and its evolution are compared in Fig. 11. The highlighted
314 regions are at the maximum degradation value of D_{post}, which indicates fracture cracking. Both
315 fracture due to local buckling at the mid-length (Figs. 11(a) and 11(b)) and fracture near the
316 stiffeners (in Fig. 11(c)), can be accurately simulated using the developed FE models. Despite
317 this, the influence of the stress intensity should be considered for a more accurate prediction of
318 the fracture propagation. This can be achieved by adapting the mesh during the simulation to
319 result in a more refined mesh adjacent to the crack tip, which is beyond the scope of this study.

320 # 3. Parametric Study and Fracture Life

321 Previous experimental studies [1-7, 9, 12] have demonstrated that the fracture life of individual
322 bracing members is influenced by both the specimen geometry (i.e. global and local
323 slendernesses) and material properties. To assist in the quantification of the brace deformation
324 and fracture life, the normalised global and local (cross-sectional) slendernesses [8], $\overline{\lambda}_G$ and
325 $\overline{\lambda}_S$, are introduced, as given by Eqs. (16) and (17), respectively.

326 $$\overline{\lambda}_G = \frac{KL/r}{\lambda_{limit}} \tag{16}$$

327 $$\overline{\lambda}_S = \frac{B'/t}{\lambda_{hd}} \tag{17}$$

328 where K is the effective length factor, taken as 0.5 for the fixed-ended members and used in
329 the parametric study, L is the brace length, r is the radius of gyration of the brace, B' is the
330 width of the flat portion of the section as determined in Fig. 1, $\lambda_{limit} = 4\sqrt{E/f_y}$ is the brace
331 slenderness limit in an ordinary concentrically V or inverted-V braced frame in AISC 341-16
332 [8], t is the tube-wall thickness, $\lambda_{hd} = 0.65\sqrt{E/\left(R_y f_y\right)}$ is the limit on the width-to-thickness
333 ratio for highly-ductile members in AISC 341-16, E and f_y are the elastic modulus and yield
334 strength of the material, respectively, and R_y is determined as 1.4.

Tables 3-5 present the material properties and specimen matrix for the parametric study. The effect of the manufacturing processes is also considered by adopting the measured material properties of cold-formed (CF) and hot-rolled (HR) tubes [50]. The Type A loading protocol, illustrated in Fig. 1(c), was adopted in the parametric study.

Fracture prediction models have been proposed in previous work at the material- and member- levels. Those at the material-level can be categorized as (1) Physics-based, such as the Rice-Tracey model [19]; (2) phenomenological, such as the modified Mohr-Coulomb model (MMC) [39]; and (3) empirical, such as the Xue-Wierzbicki model [21]. At the member-level, the models are generally expressed in terms of the displacement ductility μ_Δ [3] and the maximum plastic hinge rotation θ_G at mid-length prior to fracture [51]. These two indices, as functions of geometry and material parameters, can provide an explicit reflection of the deformation capacity of bracing members prior to fracture. In this study, the maximum plastic hinge rotation at mid-length prior to fracture θ_G, as defined in Fig. 12(a), is adopted as a criterion to predict the fracture life of SHS bracing members, as recommended in [51]. Differences between hot-rolled and cold-formed braces have been observed in previous tests [2,7,9] and thus a parametric study was conducted using the FE model developed in this paper in order to further assess and quantify these differences.

The plastic hinge model and the relationship between the axial shortening Δ_C and θ_G at the maximum compressive displacement prior to fracture are presented in Fig. 12(b). It is assumed that the axial shortening Δ_C is only contributed to by the brace rotation at the mid-length hinge of an uncompressible brace. The relationship between Δ_C and θ_G is expressed in Eq. (18) and when the approximation of $\sin(\theta_G) \approx \theta_G$ is adopted, Eq. (18) can be simplified to Eq. (19), which coincides with the equation used by Tremblay et al. [51] for single bracing members.

$$\Delta_C = L_H\left(1-\cos\theta_G\right) \tag{18}$$

$$\Delta_C = \frac{L_H}{2}{\theta_G}^2 \tag{19}$$

The influence of the slenderness parameters $\overline{\lambda}_S$ and $\overline{\lambda}_G$ on the adopted indicator of fracture life θ_G is now estimated quantitatively. The value of θ_G is calculated from Eq. (20) without assuming the approximation of $\sin(\theta_G) \approx \theta_G$, since θ_G is no longer a small value ($\geq 10°$) from the simulation results.

$$\theta_G = \sin^{-1}(2\Delta / L_H) \tag{20}$$

where L_H is the length between the two hinges at brace ends, and Δ is the out-of-plane displacement of the brace at the mid-span.

The variation of θ_G with the two slenderness parameters $\overline{\lambda}_S$ and $\overline{\lambda}_G$ is illustrated in Figs. 13(a) and (b) respectively. The proposed relationship between θ_G and the two slenderness parameters is expressed by Eq. (21).

$$\theta_G = A_\theta \cdot \overline{\lambda}_S^{\,B_\theta} \cdot \overline{\lambda}_G^{\,C_\theta} \tag{21}$$

where A_θ, B_θ and C_θ are parameters for θ_G listed in Table 6. The range of applicability of the prediction variables in Eq. (21) is determined based on the brace geometric and material properties used in the regression analysis, as shown in Table 5 (geometry) and Tables 3 and 4 (material properties)

The rotation at the maximum compressive displacement prior to fracture θ_G decreases with $\overline{\lambda}_S$ and increases with $\overline{\lambda}_G$. A minor discrepancy between the deformation capacities of the cold-formed and hot-rolled bracing members can be observed at a global slenderness of 50 in Fig. 13(a). However, the superior deformation capacity of hot-rolled bracing members is not evident beyond a certain global slenderness value, approximately λ_{cr}, as demonstrated in Fig. 13(b), where λ_{cr} is slenderness at which the elastic buckling load is equal to the yield load, as given by $\pi\sqrt{E/f_y}$. For these slender members ($\lambda_G > \lambda_{cr}$), local buckling can be less severe. Therefore, the corner material hardening for the CF series may offer some advantages in postponing fracture initiation at the corners.

The θ_G prediction equation proposed by Tremblay *et al.* [51] for the fracture life of rectangular hollow bracing members is presented in Eq. (22), where B_1 and B_2 are the cross-sectional widths perpendicular and parallel to the buckling plane, respectively.

$$\theta_{G_Tremblay} = 0.091\left(\frac{B_1}{t}\frac{B_2}{t}\right)^{-0.1}\left(\frac{KL}{r}\right)^{0.3} \quad (22)$$

The results for θ_G from the FE analyses and the calculation equations (i.e. Eqs. (21) and (22)) are compared in Fig. 14. It should be noted that the influence of the material properties and manufacturing process on θ_G are not included in Eq. (22). This prediction equation does not therefore differentiate between braces with the same geometry but different material properties or manufacturing processes, i.e. the difference between the hot-rolled and cold-formed braces of the same geometry. Generally, Fig. 14 shows that the proposed equation, Eq. (21), can reliably predict the rotational deformation capacity θ_G of hot-rolled and cold-formed steel braces prior to fracture.

4. Structure-level Analyses and Discussion

In this section, the seismic performance of concentrically-braced frames (CBFs) subjected to a cyclic inelastic deformation history is assessed with a focus on the brace parameters, including the local and global slendernesses, material properties and fabrication process. The braces are the crucial components of CBFs that provide the energy dissipation and deformation capacity. The behaviour of the braces in the CBFs is affected by the interactions with other CBF components, i.e. the columns, beams, brace-gusset-plate connections and beam-to-column connections. The component interactions can result in unintended failure modes and limited deformation capacity, if not properly designed [52-54]. This is due to the complex interactions and boundaries between the various components. To accurately simulate the seismic behaviour of CBFs, the yield and failure hierarchy of each component should be captured by the model. However, the FE simulation of an entire CBF can be computationally very expensive. Thus, beam element fibre-based FE analysis is adopted with the fracture criterion calibrated from the aforementioned refined solid finite element models, offering a highly efficient simulation

approach to evaluate the performance of CBFs. An equivalent approach for simulating the behaviour of steel members and frames under monotonic loading conditions, in which strain limits are used to capture local buckling, is presented in [55, 56].

4.1 Modelling of two-storey braced frames incorporating the proposed member-level fracture criterion for braces

The use of fibre-based finite element models to efficiently predict and assess the seismic performance of CBFs, including the instability and fracture of braces and the strength and stiffness deterioration of connections, has been demonstrated in [57-60]. Hsiao et al. [57, 58] and Sen et al. [59, 60] successfully analysed the behaviour of special and non-ductile concentrically braced frames—SCBFs and NCBFs, respectively, in OpenSees [61]. On the basis of these established approaches, a fibre-based FE model of a two-storey braced frame incorporating the member-level fracture criterion proposed herein was established using OpenSees and validated against previous experimental results [54]. Fig. 15 presents a schematic view of the model, together with the modeling details.

The beams, columns and braces were modelled using nonlinear fibre beam-column elements. One element with five integration points was used for each beam and column, whilst the brace was discretized into 16 elements with one integration point per element. The cross-sections of the beams and columns were wide-flange (W) I-sections, whilst the cross-sections of the braces were SHSs, as presented in Table 7. The cross-sections of the members were discretized into four fibres through the thickness and six fibres for each flange and web [57]. The material constitutive model of Steel02 in OpenSees [61] was adopted in the FE model. The material parameters for the beams, columns and braces were obtained from material coupon tests, as summarised in Table 7 [54].

The connecting regions between the beams, columns and braces were modelled using very stiff elastic elements (i.e., an elastic modulus 10^3 times that of the original material), as shown in Fig. 15. The lengths of these essentially rigid elements were determined based on the geometry of the adjacent gusset plates as shown in Fig. 15 [57,59]. The performance of gusset

connections would have some influence on the brace behaviour in a frame [57,59,62]. Therefore, Out-of-plane nonlinear rotational springs and in-plane nonlinear axial springs were adopted between the brace end and the gusset plate to account for the out-of-plane rotational deformation and in-plane yielding of the brace-end gusset plate, respectively, as shown in Fig. 15(b). Both the rotational and axial springs were modelled using zero-length nonlinear spring elements in OpenSees. The constitutive model of Steel02 [61] was used for the springs. The stiffness and yield moment of the nonlinear rotational springs were calculated using Eqs. (23) and (24), respectively [57].

$$K_{\text{rot}} = \frac{E}{L_{\text{ave}}}\left(\frac{W_{\text{w}} {t_{\text{g}}}^3}{12}\right) \tag{23}$$

$$M_{\text{y}} = f_{\text{y}}\left(\frac{W_{\text{w}} {t_{\text{g}}}^2}{6}\right) \tag{24}$$

The stiffness and yield force of the nonlinear axial springs were calculated using Eqs. (25) and (26), respectively [59].

$$K_{\text{axi}} = \frac{EB_{\text{w}} t_g}{L_{\text{ave}}} \tag{25}$$

$$P_{\text{y}} = f_{\text{y}} B_{\text{w}} t_{\text{g}} \tag{26}$$

where t_{g} is the thickness of the gusset plate, f_{y} is the yield stress of the gusset plate and L_{ave} and $W_{\text{w}}/B_{\text{w}}$ are the length and width parameters [57,59] for the gusset-plate connection, respectively. In-plane rotational springs, the properties of which were taken from [63], were used to describe the behaviour of the beam-to-column connections.

An initial global imperfection was introduced into the bracing members using a sinusoidal function with an amplitude of $L/500$, where L is the brace length. This amplitude is approximately equal to the mean value for hot-rolled and cold-formed hollow section members recommended as an equivalent geometric imperfection, incorporating the effects of both out-of-straightness and residual stresses, by Walport et al. [64]. The proposed fracture criterion in Eq. (21) was adopted to simulate brace fracture. The fracture prediction was readily realized

by comparing the brace end rotation with the maximum rotation criterion in Eq. (21). The simulation was terminated when the rotation reached that of the fracture criterion.

4.2 Validation

The capability of the developed fibre-based finite element models to capture the complex nonlinear behaviour and yield and failure hierarchy of CBFs was verified against cyclic test results on two-storey chevron CBFs [54]. Two test specimens—TNCBF1-N-HSS with non-compact braces (i.e. not satisfying the requirements for a moderately-ductile section in AISC 341-16 [8]) and TNCBF1-R-HSS with compact braces (i.e. satisfying the highly-ductile section requirements in AISC 341-16 [8])—were numerically replicated in OpenSees. As noted by Sen [59], these two selected specimens demonstrated complex nonlinear behaviour, suitable for validating the capacity of models to simulate various yield and failure mechanisms. The simulation results, in terms of the hysteretic curves of the base shear force versus the first-floor drift ratio and brace fracture, are compared with the experimental results in Fig 16. The simulation results from the FE model previously developed by Sen et al. [59], incorporating a maximum strain range fracture model (a fracture model at the material-level), are also presented in Figs. 16 (a) and (b). The adopted member-level fracture criterion was used to determine the maximum brace rotation before fracture of the corners of the braces (i.e. the first failure of an element in the model). The fracture points reported in the tests, which are marked on the experimental curves in Figs. 16(a) and (b), refer to full fracture of the flange or section of the brace. It is therefore reasonable that the point of fracture predicted by the proposed fracture criterion is one cycle earlier than the one reported in the test, as shown in Fig. 16(b). From the comparisons, it can be observed that the models can predict the nonlinear responses of CBFs and brace fracture with a reasonable level of accuracy.

4.3 Performance of braced frames with SHS braces: an illustrative example

To investigate the impact of the key design parameters, including the normalised sectional slenderness $\overline{\lambda}_S$ and normalised member global slenderness $\overline{\lambda}_G$, on the performance of braced frames, two series of two-storey braced frame models are analysed. The material properties of the hot-rolled and cold-formed braces were kept the same as those used in the solid FE models of the individual braces described earlier. The HR series refers to the frames with hot-rolled SHS braces, with an elastic modulus of 219.6 GPa and a yield stress of 478 MPa, whereas the CF series refers to the frames with cold-formed SHS braces, with an elastic modulus of 212.9 GPa and a yield stress of 451 MPa. The validated FE model of the TNCBF1-R-HSS test frame was adopted as the reference frame in the parametric study. The cross-sections of the beams and columns were kept the same as those in the reference frame, whilst the cross-sections and lengths of the braces were varied. The width, thickness and length of the braces were varied from 50 to 100 mm, 3.58 to 12.13 mm, and 563 to 3799 mm, respectively, to cover a wide range of $\overline{\lambda}_S$ values from 0.7 to 1.18 and $\overline{\lambda}_G$ values from 0.35 to 2.3. For the out-of-plane rotation at the ends of the braces, the gusset plates were designed to ensure a failure mode of brace fracture, whilst the properties of the zero-length nonlinear springs were kept the same throughout the parametric study with a rotational stiffness K_{rot} of 224 kNm/rad and a yield moment M_y of 16.8 kNm [57]. The properties of the in-plane axial springs and the initial imperfections for the braces were kept consistent with the validated FE model of the TNCBF1-R-HSS test frame.

The analyses were performed using OpenSees incorporating the proposed brace fracture criterion. The Type A loading protocol, as presented in Fig. 1(c), was adopted and converted to the corresponding drift demands in the fibre-based FE models (i.e. controlling the drift angle demands of the first floor) through the following relationship [65]:

$$\theta_s = \Delta / L\cos^2 45° = 2\Delta / L \tag{27}$$

where L is the first floor brace length, Δ is the axial deformation in the Type A loading protocol and θ_s is the converted first storey drift angle demand. This relationship is based on a

chevron brace configuration, assuming centreline dimensions with the braces inclined at 45° and ignoring flexural deformations in the beams and columns.

Fig. 17 presents the results of maximum drift angle for the first floor θ_{s_max} from the parametric study. The dependency of θ_{s_max} on the normalised sectional slenderness $\overline{\lambda}_S$ (in Fig. 17(a)) and normalised member global slenderness $\overline{\lambda}_G$ (in Fig. 17(b)), for hot-rolled and cold-formed braces is illustrated. The maximum storey drift angle θ_{s_max} follows the tendency observed from the individual bracing member tests, in that a larger drift angle can be achieved for braces with a lower local slenderness and a higher global slenderness.

It is interesting to note from Fig. 17(a), that a bracing member at the highly-ductile section limit (i.e. $\overline{\lambda}_S \le 1.0$) may fracture prior to achieving the expected storey drift angle, θ_{s_max}, of 0.04 rad, which is the requirement for highly-ductile members (AISC 341-16 [8]). As anticipated, the storey drift angle capacity increases with member slenderness due to the improved brace deformation capacity. However, as indicated in Fig. 17(b), CBFs with slender braces, for which the global slenderness exceeds $4\sqrt{E/f_y}$, may still not meet the requirement of a 0.04 rad storey drift angle, even with highly-ductile sections. This can be attributed to the local buckling-induced premature fracture in the corner regions. This local buckling induced fracture is indicated in the fibre-based finite element models using the proposed member-level fracture criterion, which was determined based on the global brace rotation at the onset of corner crack initiation. Furthermore, even for a requirement of a 0.02 rad storey drift angle, some bracing members with low member slenderness that meet the moderately ductile section criterion may still fail to survive at this drift value prior to fracture, as shown in both Figs. 17 (a) and (b).

In the AISC seismic design provisions [8], the member and cross-sectional slenderness limits are determined separately. However, from the experimental observations [1-7], the interactive effects of global and local bucking should be considered in the assessment of fracture life. It is explicitly demonstrated in the proposed Eq. (21) that the deformation capacity

536 of a bracing member is governed by both the local and global slenderness parameters, $\overline{\lambda}_S$ and
537 $\overline{\lambda}_G$, as well as the material properties.

538 It should be noted that the established fibre-based FE models are based on quasi-static
539 analyses. The dynamic effects will be addressed in a future study by adopting real and artificial
540 ground motion excitations to advance the knowledge and evaluation of the seismic
541 performance of the braced frames. Despite this, the results presented in this study illustrate that
542 the section slenderness limits in the current seismic design provision may need to be tightened.

543 # 5. Conclusions

544 The hysteretic and fracture behaviour of cyclically loaded square hollow section (SHS) braces
545 and corresponding concentrically braced frames has been modelled and assessed. Both
546 member-level (solid finite element models) and structure-level (fibre-based finite element
547 models) simulations incorporating fracture criteria have been established to evaluate the effects
548 of various geometric and material parameters on the extremely low cycle fatigue fracture of
549 bracing members. The following conclusions can be drawn from this study within the validity
550 range of the parametric analysis:

551 1) A material-level fracture criterion and nonlinear damage evolution rule have been
552 employed in solid FE models of individual braces. The FE models of SHS braces were
553 validated against test results and could predict buckling-induced fracture, including
554 crack initiation and propagation, under extremely low cycle fatigue (ELCF) accurately
555 for both hot-rolled and cold-formed bracing members.

556 2) The coupled effects of buckling and ductile fracture on the rotational deformation
557 capacity of cyclically loaded braces prior to fracture were quantified in terms of the
558 normalised cross-sectional and global slendernesses using a plastic-hinge based
559 analytical model. The effects of the geometry, material properties and manufacturing
560 process on the fracture life of bracing members were included. It should also be noted

that the proposed prediction equation for brace fatigue life was derived based on the ECCS loading protocol, and its suitability for application should be further verified.

3) The cross-sectional and member slendernesses were found to have a different influence on the deformation capacity of the braces prior to fracture. Bracing members with stocky sections and large global slenderness values tended to possess superior global deformation capacity.

4) For members with low global slenderness, the hot-rolled SHS braces exhibited slightly higher deformation capacity compared to their cold-formed counterparts. In contrast, for members of high global slenderness, the cold-formed braces tended to have longer fracture lives.

5) In the structure-level analyses, the brace rotation capacity prior to fracture was employed as a member fracture criterion. The fibre-based FE models with the member-level fracture criterion were validated against experimental results on two-storey braced frames. Comparisons showed that the models can provide reasonable predictions of the fracture of the brace members within a structural subassembly.

6) The maximum storey drift angle of a two-storey chevron-braced frame was assessed based on a structure-level parametric study using the fibre-based finite element models. Based on the numerical results, it is recommended that the interactive effects of global and local buckling are considered when developing cross-sectional slenderness limits of braces for a given ductility level.

Acknowledgments

The research work presented in this paper was supported by the Chinese National Engineering Research Centre for Steel Construction (Hong Kong Branch) at The Hong Kong Polytechnic University. The first author would like to acknowledge the financial support from JSPS KAKENHI Grant Number 19F19360. Support from Dr. K.H. Nip for providing essential

586 experimental data and Dr. Andrew D. Sen for helping with the braced frame modelling scheme
587 are also gratefully appreciated.

References

[1] Tremblay R. Inelastic seismic response of steel bracing members. Journal of Constructional Steel Research 2002; 58(5-8):665-701.

[2] Nip KH, Gardner L, Elghazouli AY. Cyclic testing and numerical modelling of carbon steel and stainless steel tubular bracing members. Engineering Structures 2010; 32(2):424-441.

[3] Fell BV. Large-scale testing and simulation of earthquake-induced ultra low cycle fatigue in bracing members subjected to cyclic inelastic buckling. Ph.D. thesis, University of California, Davis, 2008.

[4] Shaback B, Brown T. Behaviour of square hollow structural steel braces with end connections under reversed cyclic axial loading. Canadian Journal of Civil Engineering 2003; 30(4):745-53.

[5] Goggins JM, Broderick BM, Elghazouli AY, Lucas AS. Experimental cyclic response of cold-formed hollow steel bracing members. Engineering Structures 2005; 27(7):977-89.

[6] Elchalakani M, Zhao XL, Grzebieta R. Tests of cold-formed circular tubular braces under cyclic axial loading. Journal of Structural Engineering 2003; 129(4):507-514.

[7] Sheehan T, Chan TM. Cyclic response of hollow and concrete-filled circular hollow section braces. Proceedings of the ICE – Structures and Buildings 2014; 167(3):140-152.

[8] AISC 341. Seismic provisions for structural steel buildings. AISC-341, Chicago, 2016.

[9] Packer JA, Chiew SP, Tremblay R, Martinez-Saucedo G. Effect of material properties on hollow section performance. Proceedings of the ICE - Structures and Buildings 2010; 163(6):375-390.

[10] Meng X and Gardner L. Behavior and design of normal and high strength steel SHS and RHS columns. Journal of Structural Engineering, ASCE 2020; 146(11):04020227.

[11] Yaghoubshahi M, Imanpour A. An overview of HSS brace fracture in steel concentrically braced frames. Journal of Constructional Steel Research 2021; 185(5) :106845.

[12] Uriz P. Towards earthquake resistant design of concentrically braced steel structures. Ph.D. Thesis, University of California, Berkeley, 2005.

[13] Coffin JL. A study of the effect of cyclic thermal stresses on a ductile metal. American Society Mechanical Engineering 1954; 76:931-50.

[14] Manson SS. Behaviour of materials under conditions of thermal stress. NACA TN 2933; 1953.

[15] Wen HJ, Mahmoud H. A new approach to predict cyclic response and fracture of shear links and eccentrically braced frames. Frontiers in Built Environment 2018; (4):11.

[16] Xu F, Chan TM, Sheehan T, Gardner L. Prediction of ductile fracture for circular hollow section bracing members under extremely low cycle fatigue. Engineering Structures 2020; 214:110579.

[17] Kanvinde AM, Deierlein GG. Cyclic void growth model to assess ductile fracture initiation in structural steels due to ultra low cycle fatigue. Journal of Engineering Mechanics 2007; 133(6):701-712.

[18] McClintock FA. A criterion for ductile fracture by the growth of holes. Journal of Applied Mechanics 1968; 35:363-371.

[19] Rice JR, Tracey DM. On the ductile enlargement of voids in triaxial stress fields. Journal of the Mechanics and Physics of Solids 1969; 17:201-217.

[20] Bai YL, Wierzbicki T. A new model of metal plasticity and fracture with pressure and Lode dependence. International Journal of Plasticity 2008; 24(6):1071-1096.

[21] Xue L, Wierzbicki T. Ductile fracture initiation and propagation modeling using damage plasticity theory. Engineering Fracture Mechanics 2008; 75(11):3276-3293.

[22] Barsoum I, Jonas F. Rupture mechanisms in combined tension and shear -Experiments. International Journal of Solids and Structures 2007; 44(6):1768-1786.

[23] Kiran R, Khandelwal K. A triaxiality and Lode parameter dependent ductile fracture criterion. Engineering Fracture Mechanics 2014; 128:121-138.

[24] Smith CMA. Stress-Weighted Damage Model for Ductile Fracture Initiation in Structural Steel under Cyclic Loading and Generalized Stress States. Ph.D. thesis, Stanford University, 2013.

[25] Bai YL. Fracture of 1045 steel under complex loading history. AIP Conf. Proc. Vol. 1383, 58-746:2011.

[26] Algarni M, Choi Y, Bai YL. A unified material model for multiaxial ductile fracture and extremely low cycle fatigue of Inconel 718. International Journal of Fatigue 2017; 96:162-177.

[27] Pack K, Marcadet S. Numerical failure analysis of three-point bending on martensitic hat assembly using advanced plasticity and fracture models for complex loading. International Journal of Solids and Structures 2016; 85:144-159.

[28] Wen HJ, Mahmoud H. New model for ductile fracture of metal alloys. II: Reverse loading. Journal of Engineering Mechanics 2015; 142(2):04015089.

[29] Kanvinde AM. Predicting Fracture in Civil Engineering Steel Structures: State of the Art. Journal of Structural Engineering 2016; 143:03116001.

[30] Rasmussen K, Hancock GJ. Design of cold-formed stainless steel tubular members. ii: beams. Journal of Structural Engineering 1993; 119(8) :2368-2386.

[31] Cruise RB, Gardner L. Strength enhancements induced during cold forming of stainless steel sections. Journal of Constructional Steel Research 2008; 64(11):1310-1316.

[32] Theofanous M, Gardner L. Testing and numerical modelling of lean duplex stainless steel hollow section columns. Engineering Structures 2009; 31(12):3047-3058.

[33] Huang Y, Young B. The art of coupon tests. Journal of Constructional Steel Research 2014; 96:159-175.

[34] ABAQUS 6.14 [Computer software]. Dassault Systems, Waltham, MA, USA; 2014.

[35] ECCS. Recommended testing procedure for assessing the behaviour of structural steel elements under cyclic loads. European Convention for Constructional Steelwork 1986, Brussels, Belgium.

[36] Hibbitt HD, Karlsson BI, Sorensen P. ABAQUS documentation collection. Ver. 6.14, USA; 2014.

[37] Lemaitre J, Chaboche JL, Mechanics of Solid Materials, Cambridge University Press, 1990.

[38] Rossi B, Afshan S, Gardner L. Strength enhancements in cold-formed structural sections—Part II: Predictive models. Journal of Constructional Steel Research 2013; 83:189-96.

[39] Bai YL, Wierzbicki T. Application of extended Mohr–Coulomb criterion to ductile fracture. International Journal of Fracture 2010; 161(1):1-20.

[40] Xu F, Chen J, Chan TM. Mechanical behaviour of concrete-filled CHS connections subjected to in-plane bending. Engineering Structures 2017; 148:101-112.

[41] Xu F, Chen J, Chan TM. Numerical analysis and punching shear fracture based design of longitudinal plate to concrete-filled CHS connections. Construction and Building Materials 2017; 156:91-106.

[42] Xu F, Chen J, Jin WL. Punching shear failure of concrete-filled steel tubular CHS connection. Journal of Constructional Steel Research 2016; 124:113-121.

[43] Xu F., Chen, J., Shu, K. and Su, M.N. Cyclic behaviour of double-tube buckling-restrained braces for boiler steel plant structures. Journal of Constructional Steel Research 2018, 150:556-569.

[44] Hollomon JH. Tensile Deformation. Transactions of the Metallurgical Society of AIME 1945; 162:268-290.

[45] Swift HW. Plastic instability under plane stress. Journal of the Mechanics and Physics of Solids 1952; 1(1):1-18.

[46] Coulomb CA. Essai sur une application des regles des maximis et minimis a quelquels problemesde statique relatifs, a la architecture. Mem. Acad. Roy. Div. Sav. 1776; 7:343–387.

[47] Amiss JM, Jones FD, Ryffel HH, McCauley CJ. Guide to the use of tables and formulas in machinery's handbook, Industrial Press, New York, USA; 2004.

[48] Wierzbicki T, Bao YB, Lee YW, Bai YL. Calibration and evaluation of seven fracture models. International Journal of Mechanical Sciences 2005; 47(4):719-743.

[49] Bai YL, Atkins T. Tension and shear cracking during indentation of ductile materials by opposed wedges. Engineering Fracture Mechanics 2012; 96:49-60.

[50] Nip KH, Gardner L, Davies CM, Elghazouli AY. Extremely low cycle fatigue tests on structural carbon steel and stainless steel. Journal of Constructional Steel Research 2010; 66(1):96-110.

[51] Tremblay R, Archambault MH, Filiatrault A. Seismic response of concentrically braced steel frames made with rectangular hollow bracing members. Journal of Structural Engineering 2003; 129(12):1626-1636.

[52] Roeder CW, Lumpkin EJ, Lehman DE. A balanced design procedure for special concentrically braced frame connections. Journal of Constructional Steel Research 2011; 67(11), 1760-1772.

[53] Hsiao PC, Lehman DE, Berman JW, Roeder C, Powell J. Seismic vulnerability of older braced frames. Journal of Performance of Constructed Facilities 2012; 28(1) :108-120.

[54] Sen AD, Roeder C, Berman J, Lehman D, Li CH, Wu AC. Tsai KC. Experimental investigation of chevron concentrically braced frames with yielding beams. Journal of Structural Engineering 2016; 142(12), 04016123.

[55] Fieber A, Gardner L, Macorini L. Design of structural steel members by advanced inelastic analysis with strain limits. Engineering Structures. 2019; 199:109624.

[56] Fieber A, Gardner L, Macorini L. Structural steel design using second-order inelastic analysis with strain limits. Journal of Constructional Steel Research. 2020; 168:105980.

[57] Hsiao PC, Lehman DE, Roeder CW. Improved analytical model for special concentrically braced frames. Journal of Constructional Steel Research 2012; 73:80-94.

[58] Hsiao PC, Lehman DE, Roeder CW. A model to simulate special concentrically braced frames beyond brace fracture. Earthquake Engineering and Structural Dynamics 2013; 42(2):183-200.

[59] Sen AD, Roeder CW, Lehman DE, Berman, JW. Nonlinear modeling of concentrically braced frames. Journal of Constructional Steel Research 2019; 157:103-120.

[60] Sen AD. New Methods for Seismic Performance Evaluation and Retrofit of Nonductile Concentrically Braced Frames, Ph.D. thesis, University of Washington, 2018.

[61] Open System for Earthquake Engineering Simulation (OpenSees). http:// opensees.berkeley.edu accessed September 2019.

[62] Bai JL, Chen HM, Zhao JX, Liu MH, Jin SS. Seismic design and subassemblage tests of buckling-restrained braced RC frames with shear connector gusset connections. Engineering Structures 2021; 234:112018.

[63] Liu J, Astaneh-Asl A. Moment–rotation parameters for composite shear tab connections. Journal of Structural Engineering 2004; 130(9):1371-1380.

[64] Walport F, Gardner L, Nethercot DA. Equivalent bow imperfections for use in design by second order inelastic analysis. Structures 2020; 26:670-685

[65] Fell BV, Kanvinde AM, Deierlein GG, Myers AT. Experimental investigation of inelastic cyclic buckling and fracture of steel braces. Journal of Structural Engineering 2009; 135(1):19-32.

List of Figure Captions

Fig. 1 Test specimens and loading protocols

Fig. 2 FE model of a quarter of a specimen

Fig. 3 Effect of element types (C3D8R and S4R) on the hysteretic response and fracture of brace specimen 40×40×3×1250-CS-HR

Fig. 4 Mesh sensitivity study

Fig. 5 Typical uniaxial stress-strain curve with progressive damage degradation [30] (Note: D refers to D_{post})

Fig. 6 Relationship between fracture index and (a) stress triaxiality and (b) normalized Lode angle at the corner region for brace specimen 40×40×3×1250-CS-HR

Fig. 7 Flow chart for the USDFLD subroutine use in the fracture model

Fig. 8 Comparison between experimental and numerical hysteretic curves for SHS brace tests reported in [2] (a~c: HR; d~g: CF)

Fig. 9 Comparison between experimental and numerical hysteretic curves for SHS brace tests reported in [3]

Fig. 10 Initiation and propagation of cyclic fracture cracks

Fig. 11 Different failure modes of SHS brace specimens [2] (a and b: Typical failure modes for fracture at mid-length - 60×60×3×2050-CS-HF; c: typical failure mode for fracture around the stiffeners - 40×40×4×2050-CS-CF)

Fig. 12 Analytical model at maximum deformation before fracture

Fig. 13 Global angle parameter θG at maximum compressive displacement prior to fracture

Fig. 14 Comparison between calculated and FE values of θ_G

Fig. 15 Fibre-based FE model of two-storey braced frame in OpenSees

Fig. 16 Comparison of experimental and numerical responses of base shear-storey drift relationship [54, 59]

Fig. 17 Maximum storey drift angle before brace fracture

List of Table Captions

Table 1. Summary of nominal dimensions and measured material properties of brace specimens

Table 2. Comparison between test and FE results

Table 3. Parameters for material model used in FE simulations

Table 4. Parameters of fracture criterion and damage evolution rule used in FE models

Table 5. Simulation matrix in parametric studies

Table 6. Parameters of proposed brace fracture initiation models

Table 7. Cross-sections and material properties of CBF members [49]

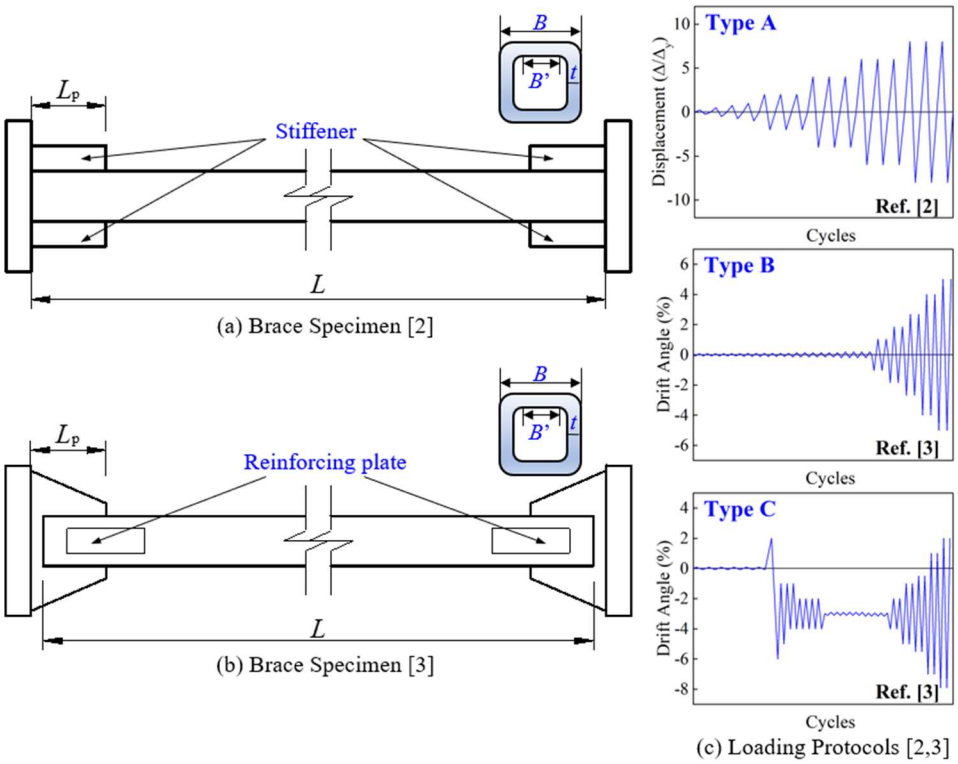


Fig. 1 Test specimens and loading protocols

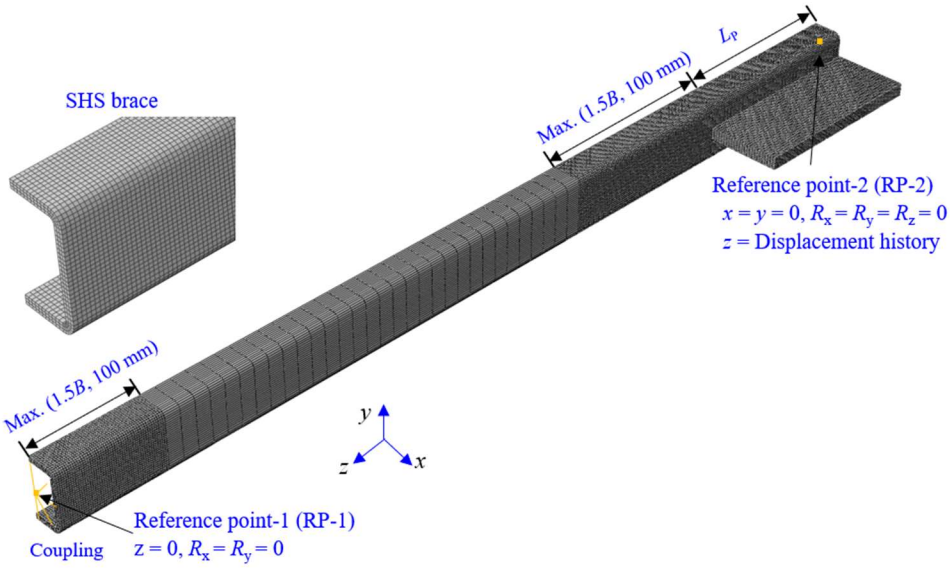


Fig. 2 FE model of a quarter of a specimen

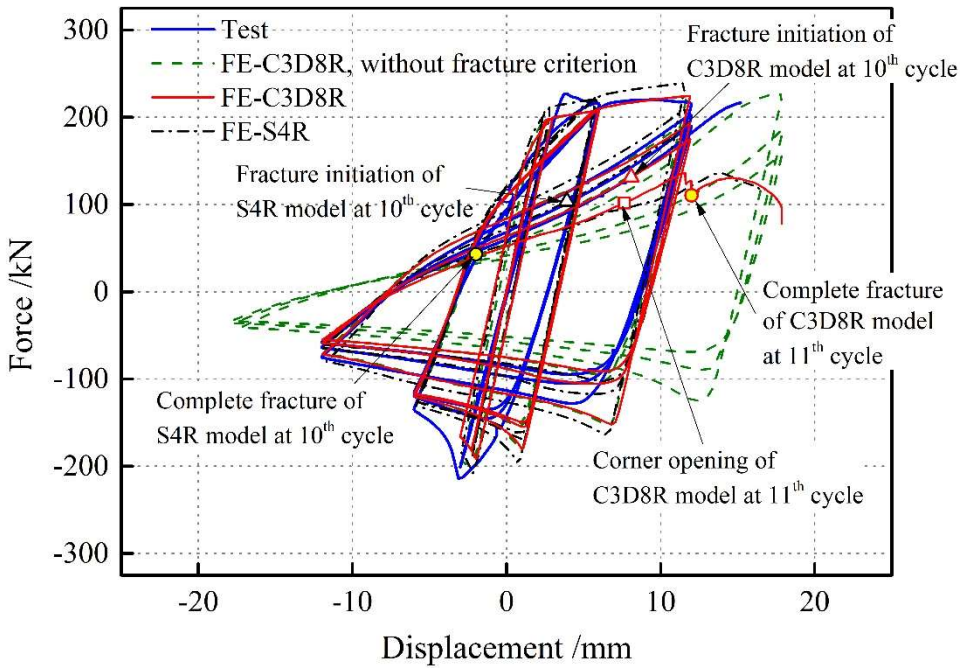


Fig. 3 Effect of element types (C3D8R and S4R) on the hysteretic response and fracture of brace specimen 40×40×3×1250-CS-HR

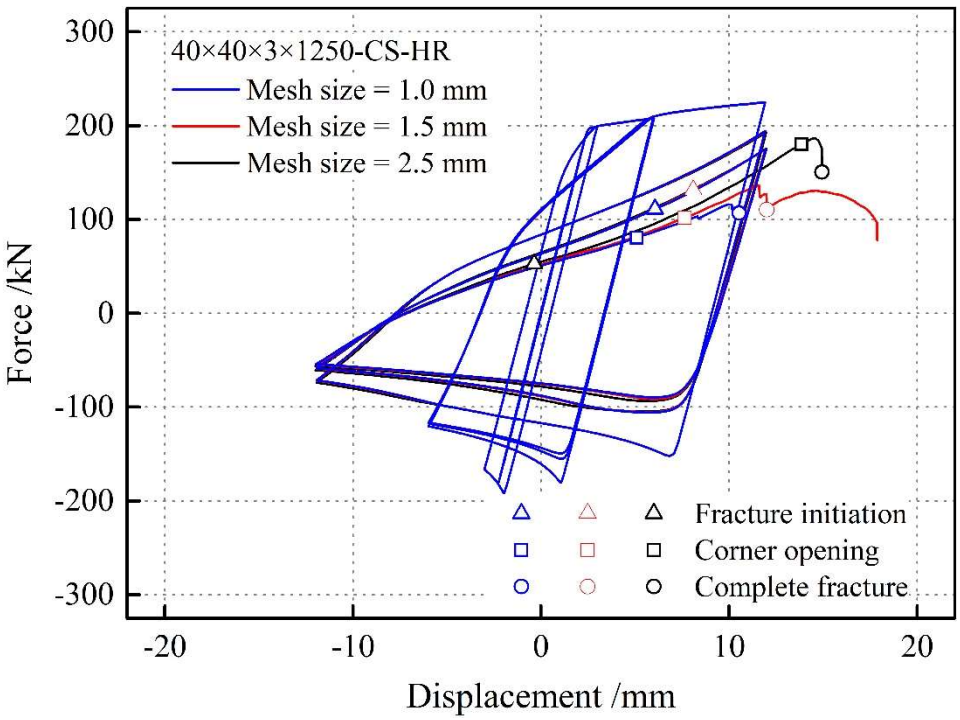


Fig. 4 Mesh sensitivity study

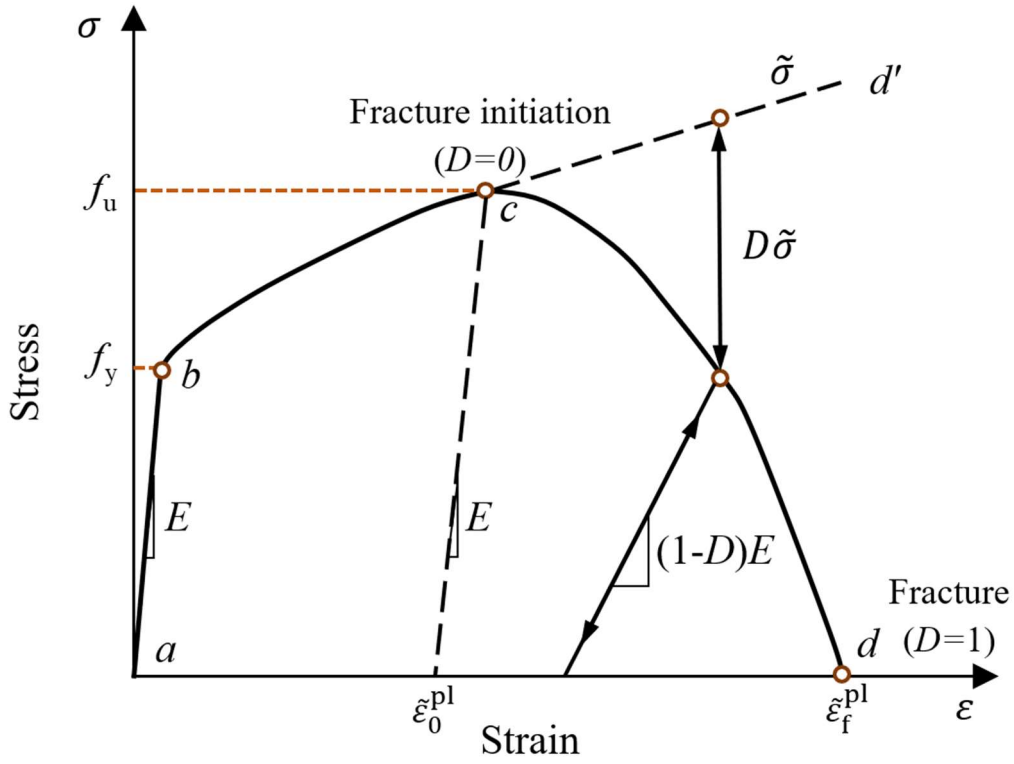
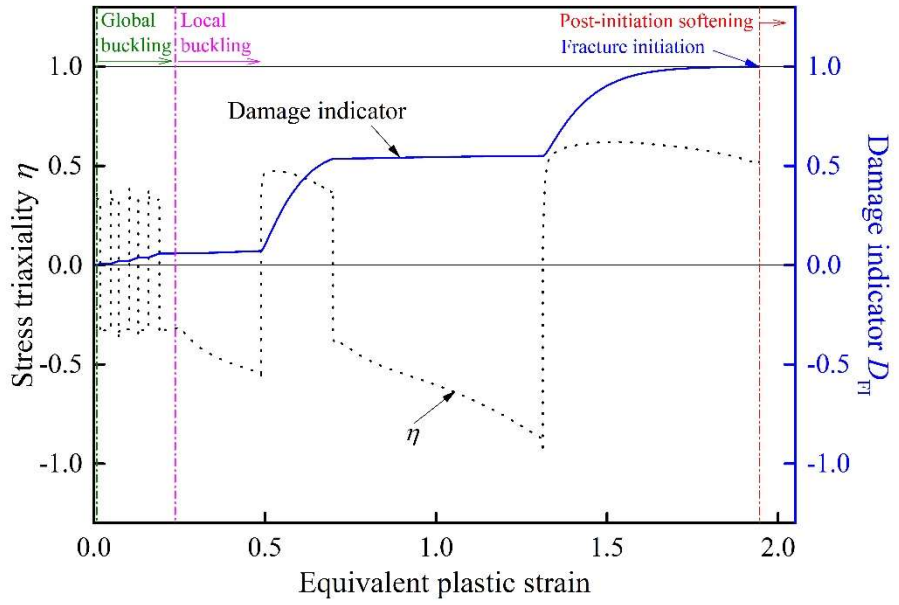
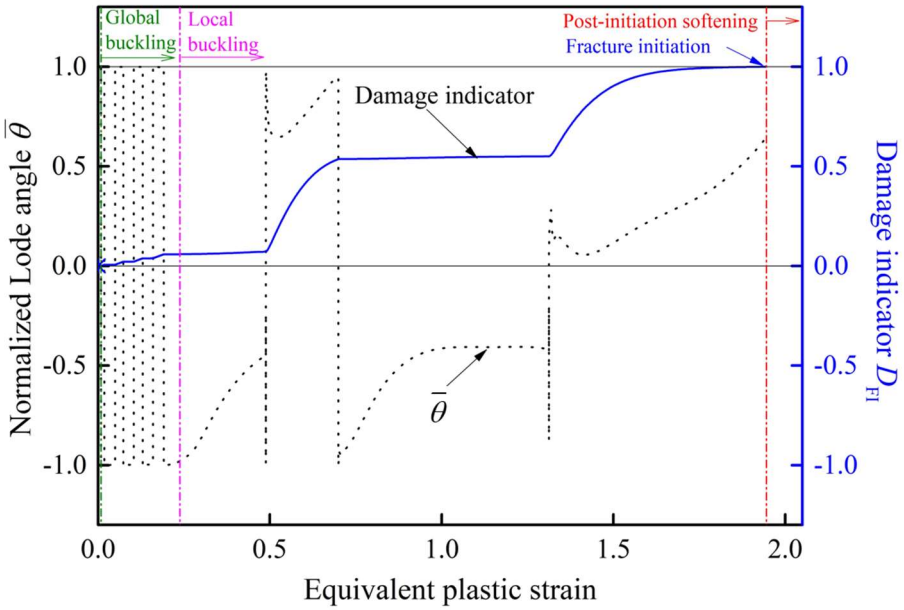


Fig. 5 Typical uniaxial stress-strain curve with progressive damage degradation [36] (Note: D refers to D_{post})



(a) Stress triaxiality



(b) Normalized Lode angle

Fig. 6 Relationship between fracture index and
(a) stress triaxiality and (b) normalized Lode angle at the corner region for brace specimen 40×40×3×1250-CS-HR

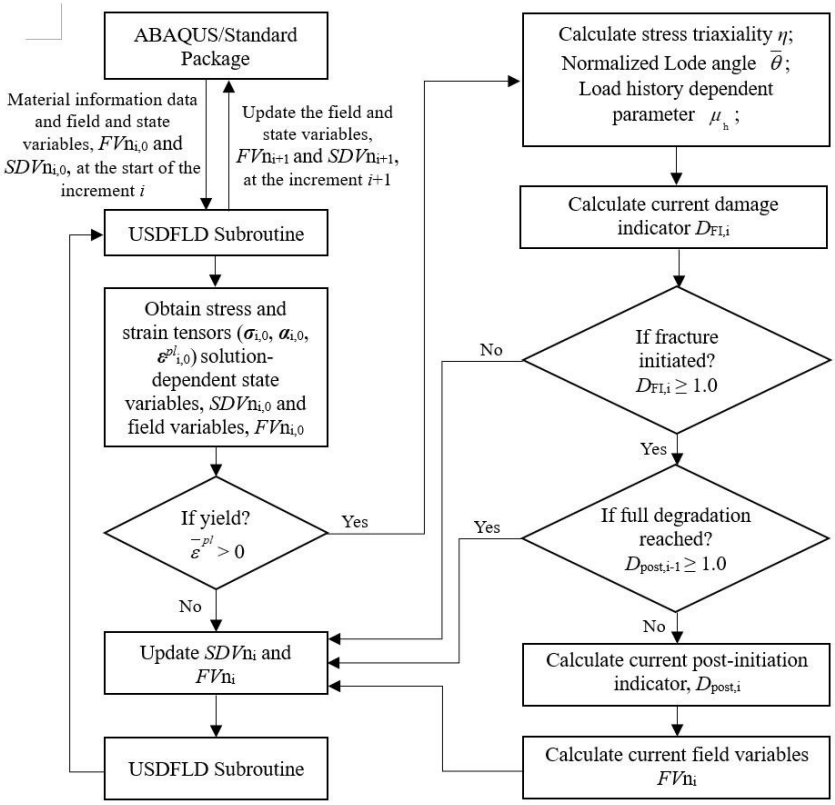
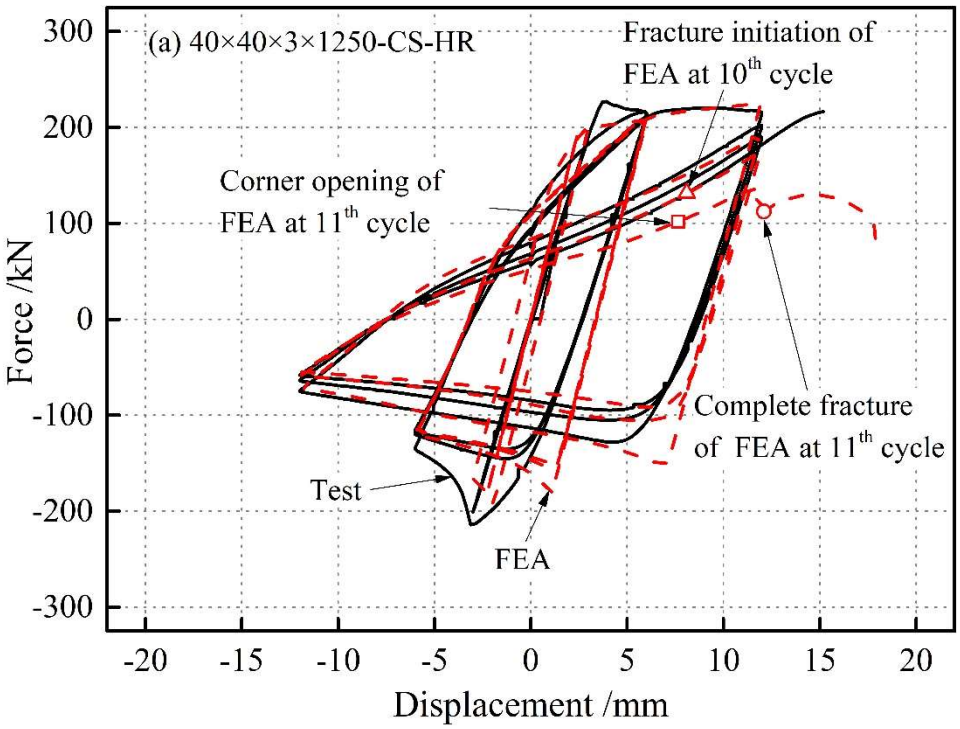
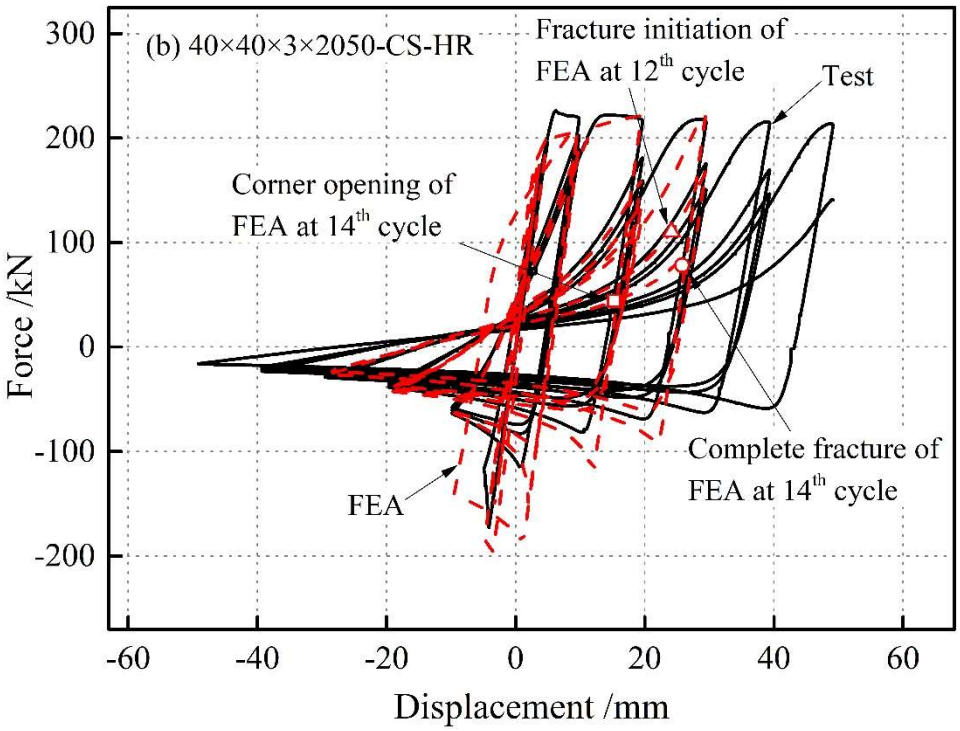


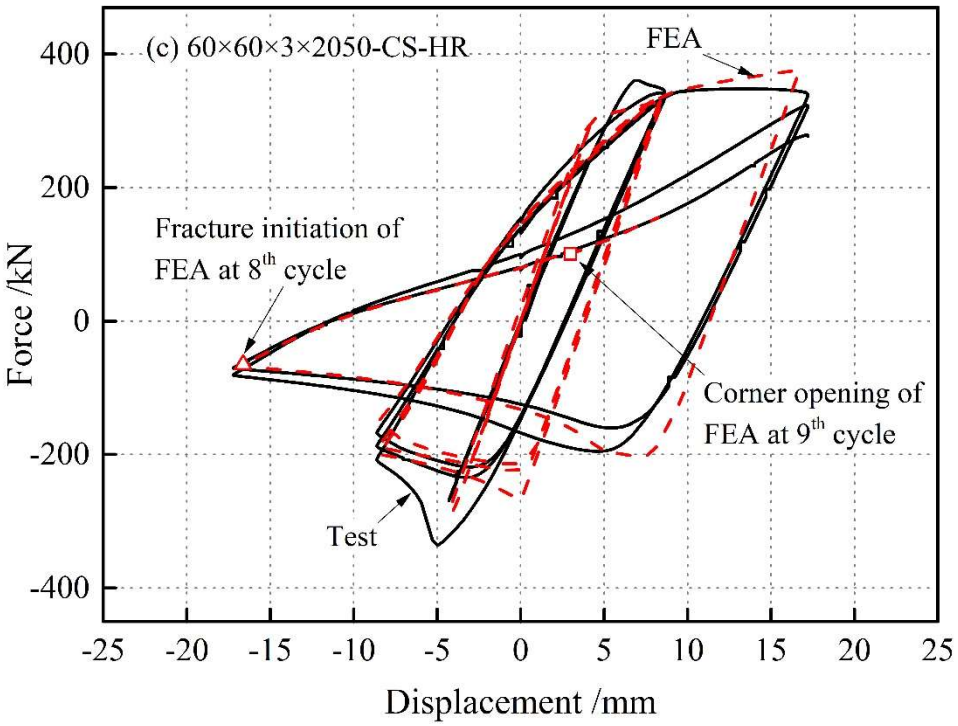
Fig. 7 Flow chart for USDFLD subroutine used in fracture model



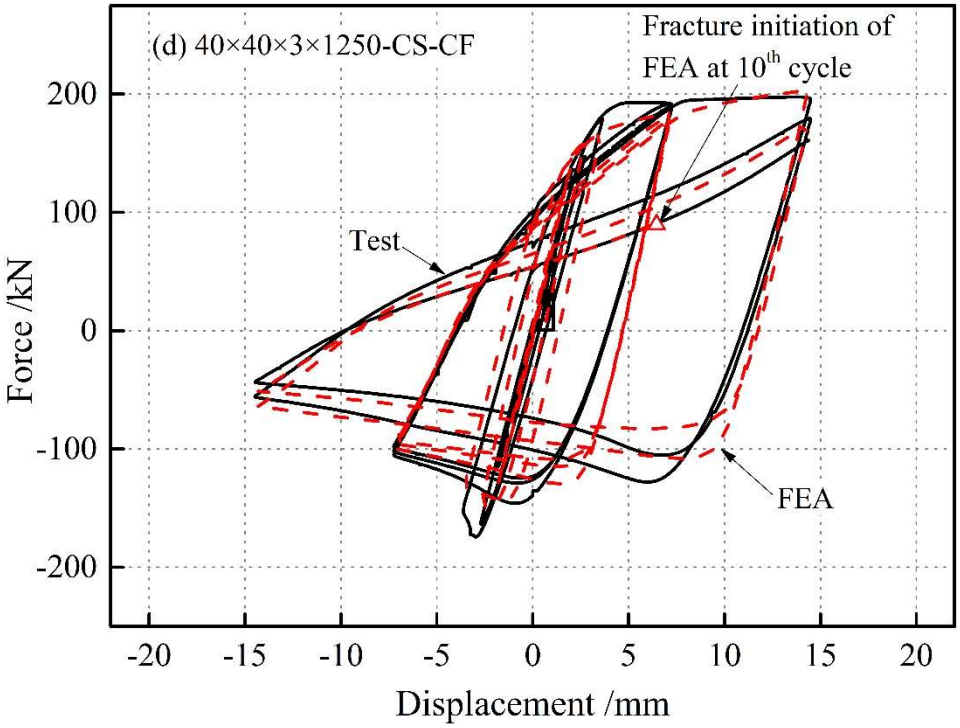
(a) 40×40×3×1250-CS-HR (Hot-rolled);



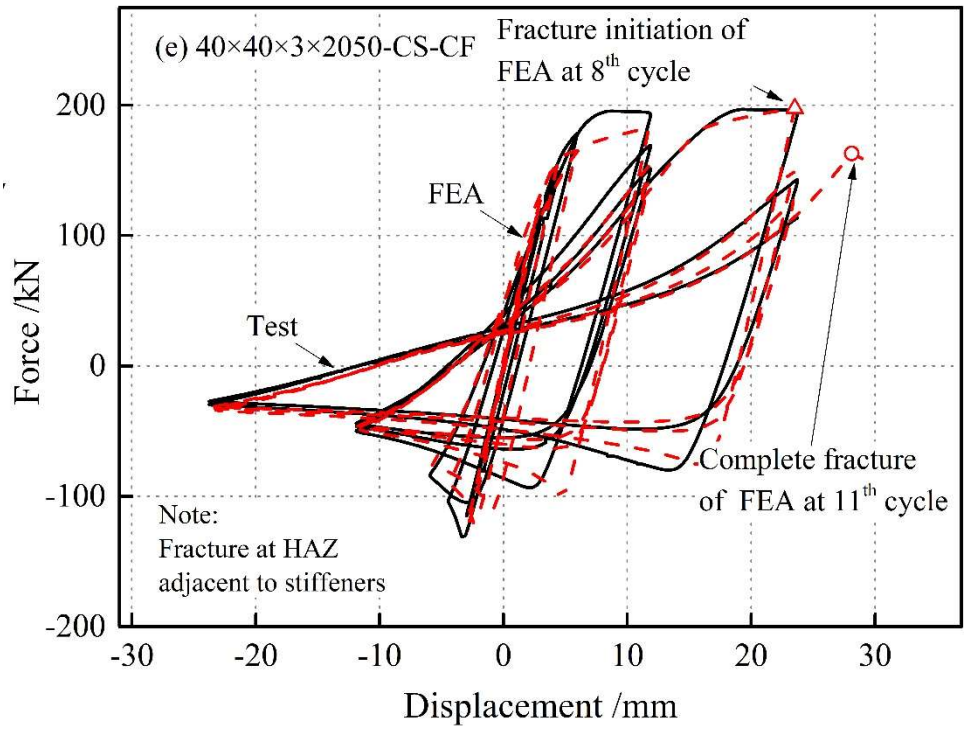
(b) 40×40×3×2050-CS-HR (Hot-rolled)



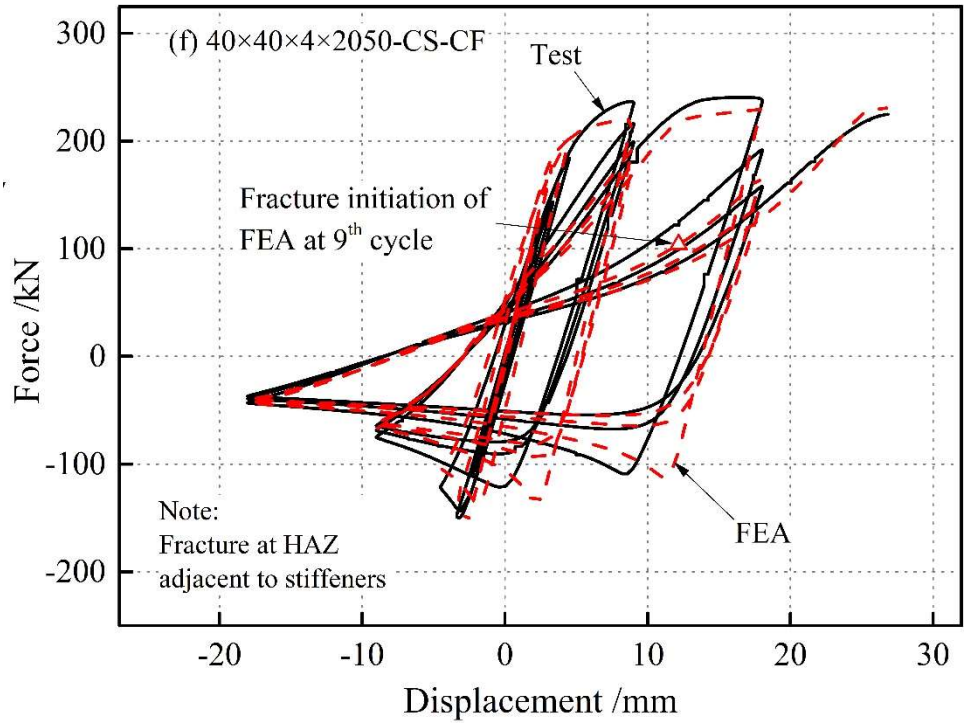
(c) 60×60×3×2050 -CS-HR (Hot-rolled)



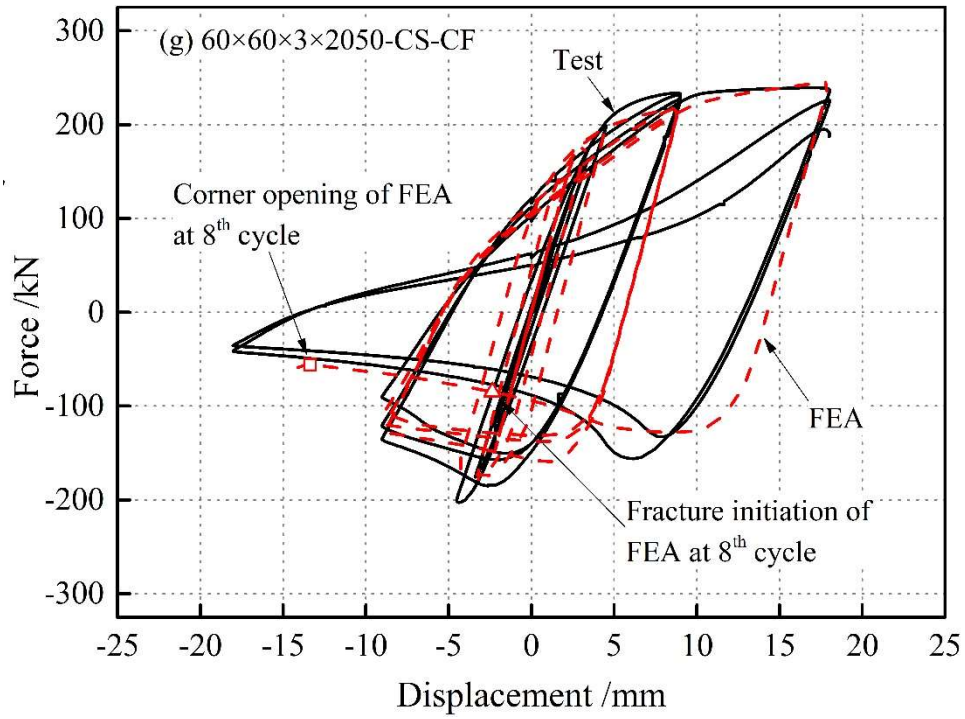
(d) 40×40×3×1250-CS-CF (Cold-formed)



(e) 40×40×3×2050-CS-CF (Cold-formed)

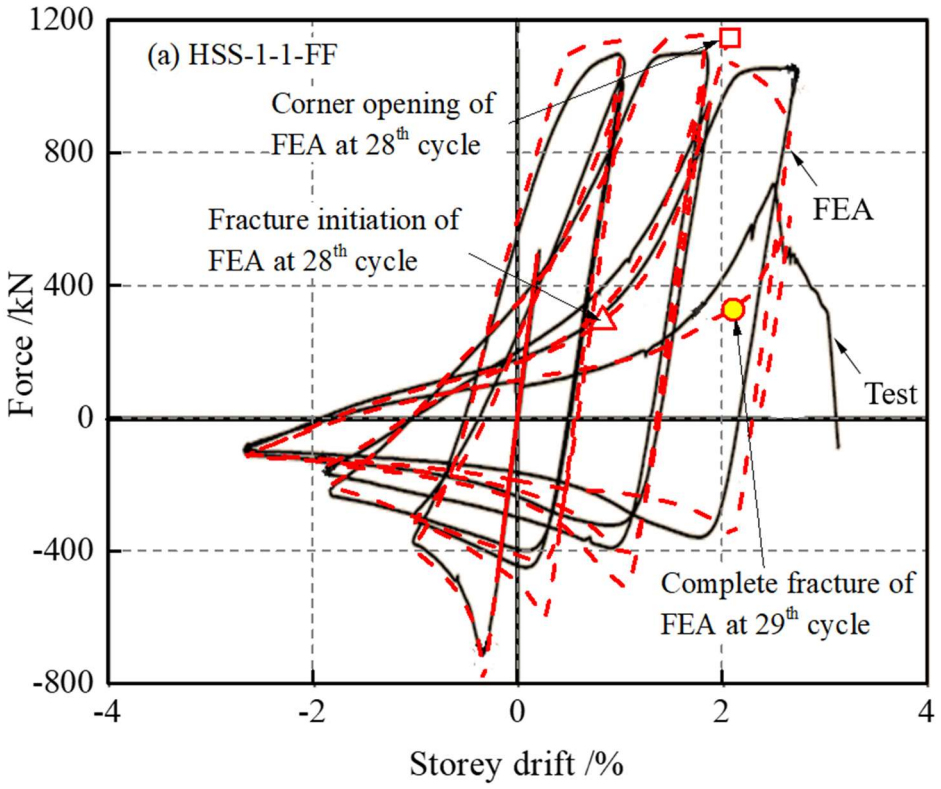


(f) 40×40×4×2050-CS-CF (Cold-formed)

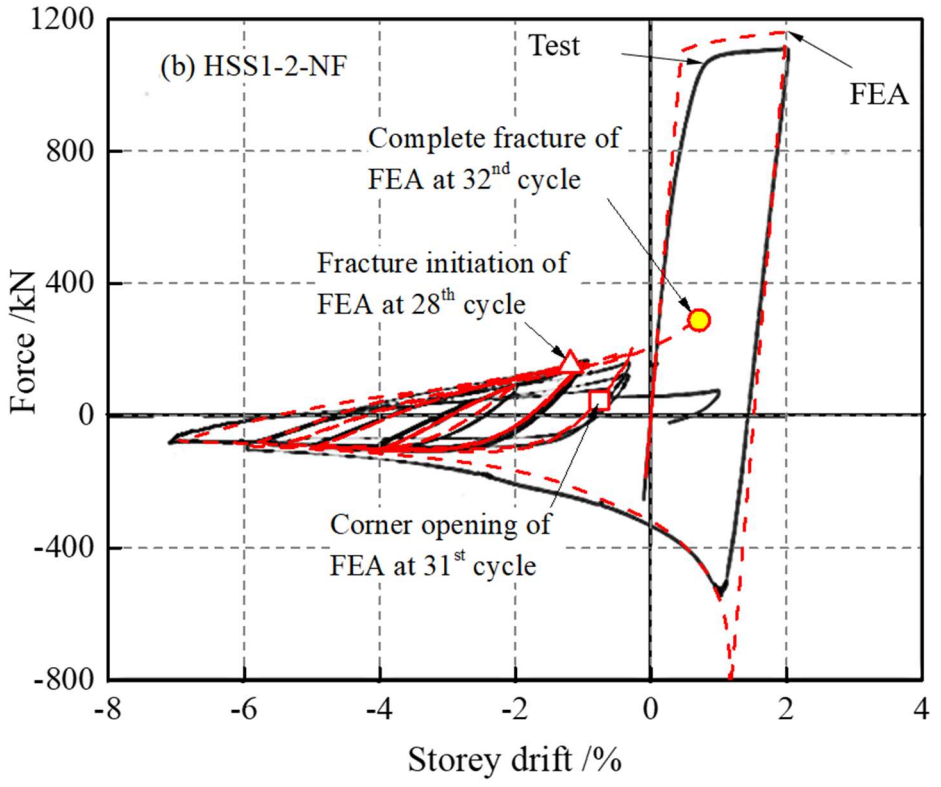


(g) 60×60×3×2050-CS-CF (Cold-formed)

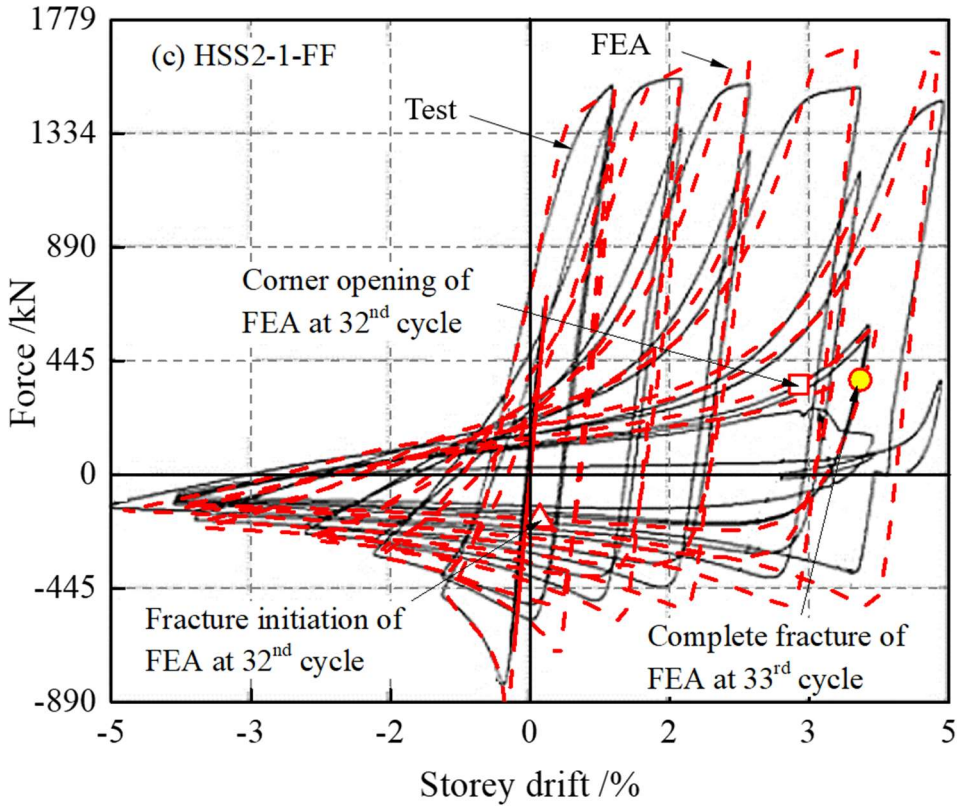
Fig. 8 Comparison between experimental and numerical hysteretic curves for SHS brace tests reported in [2] (a~c: HR; d~g: CF)



(a) HSS1-1-FF



(b) HSS1-2-NF



(c) HSS2-1-FF

Fig. 9 Comparison between experimental and numerical hysteretic curves for SHS brace tests reported in [3]

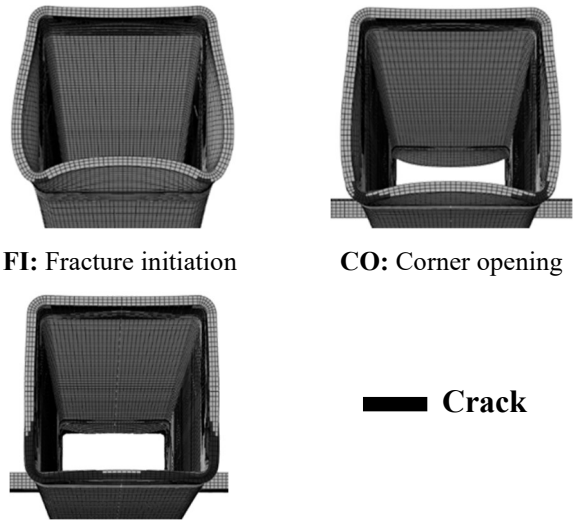
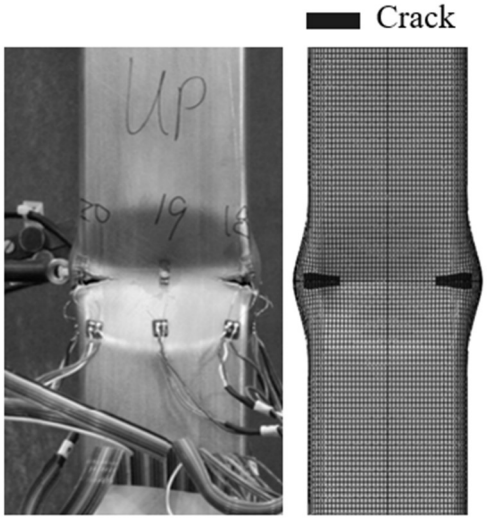
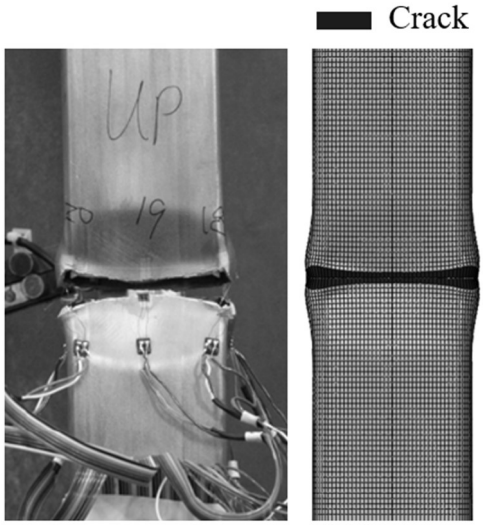


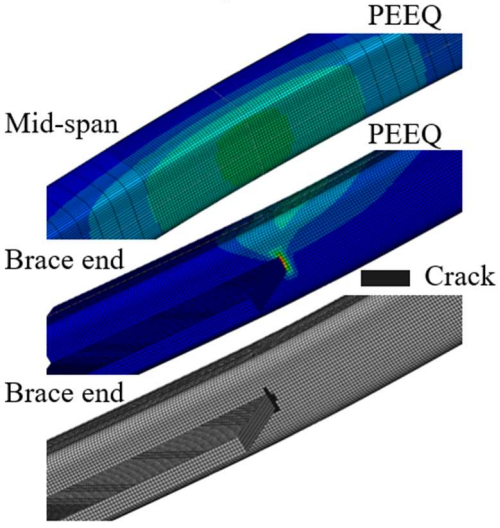
Fig. 10 Initiation and propagation of cyclic fracture cracks



(a) Corner opening



(b) Complete fracture

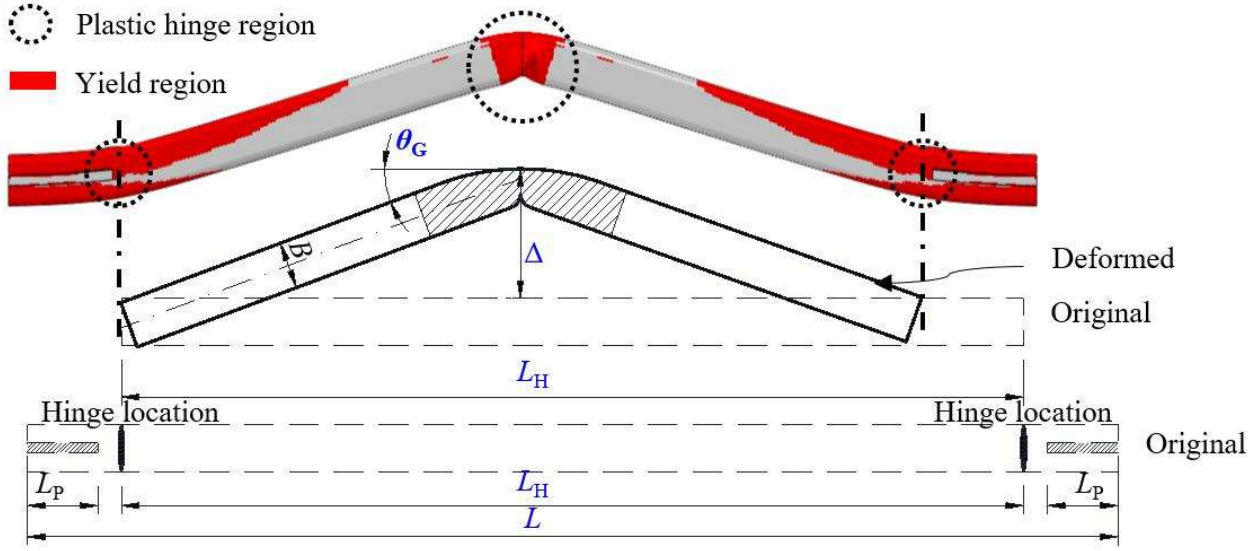


(c) Fracture at the end of the stiffener plate

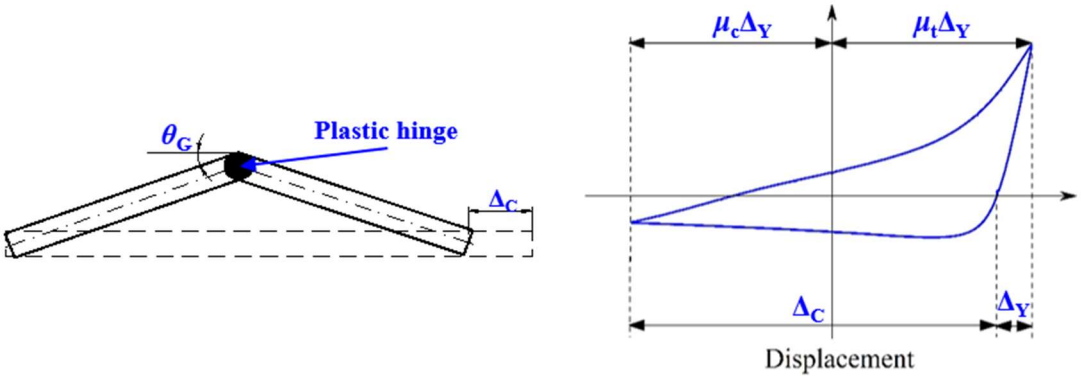
Fig. 11 Different failure modes of SHS brace specimens [2]

(a and b: Typical failure modes for fracture at mid-length - 60×60×3×2050-CS-HR;

c: typical failure mode for fracture around the stiffeners - 40×40×4×2050-CS-CF)

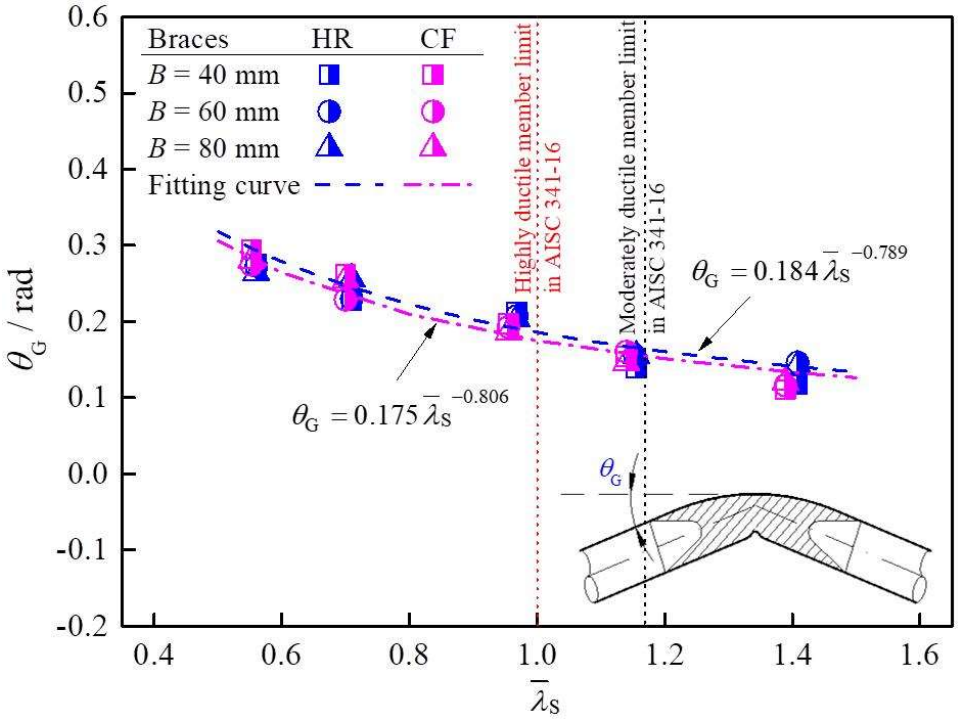


(a) Definition of rotation index θ_G

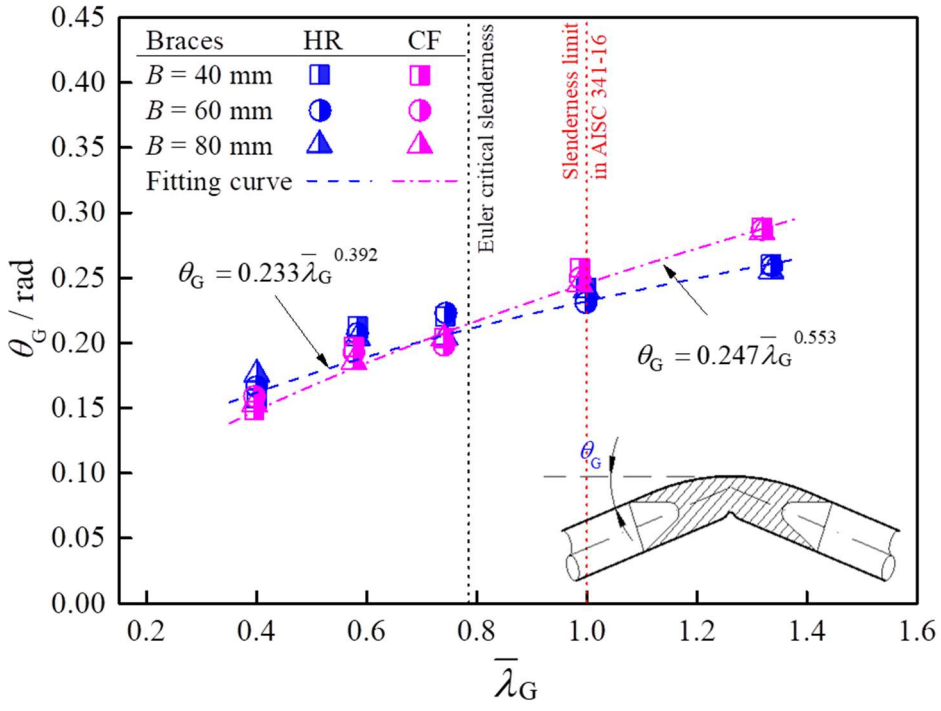


(b) Plastic hinge model

Fig. 12 Analytical model at maximum deformation before fracture



(a) Models with member slenderness $\lambda_G = \frac{KL}{r} = 50$, $\bar{\lambda}_S = \frac{B'/t}{\lambda_{hd}}$



(b) Models with cross-sectional slenderness $\lambda_S = B'/t = 11.4$, $\bar{\lambda}_G = \frac{KL/r}{\lambda_{limit}}$

Fig. 13 Global angle parameter θ_G at maximum compressive displacement prior to fracture

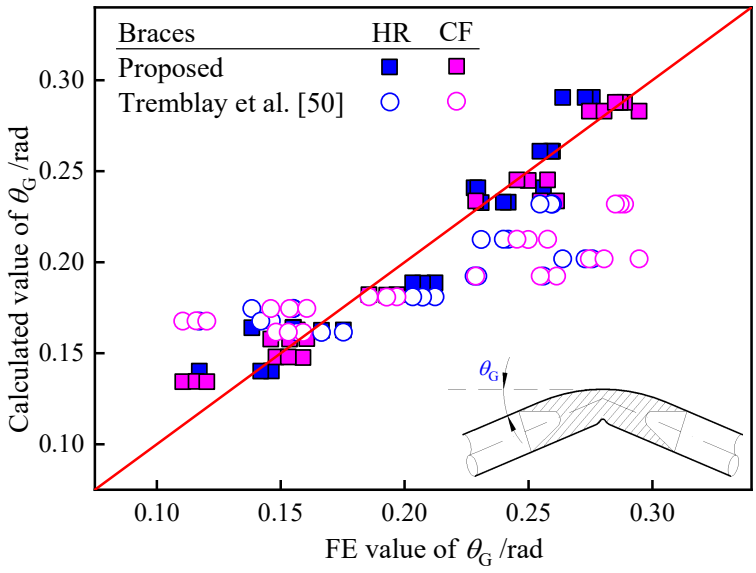
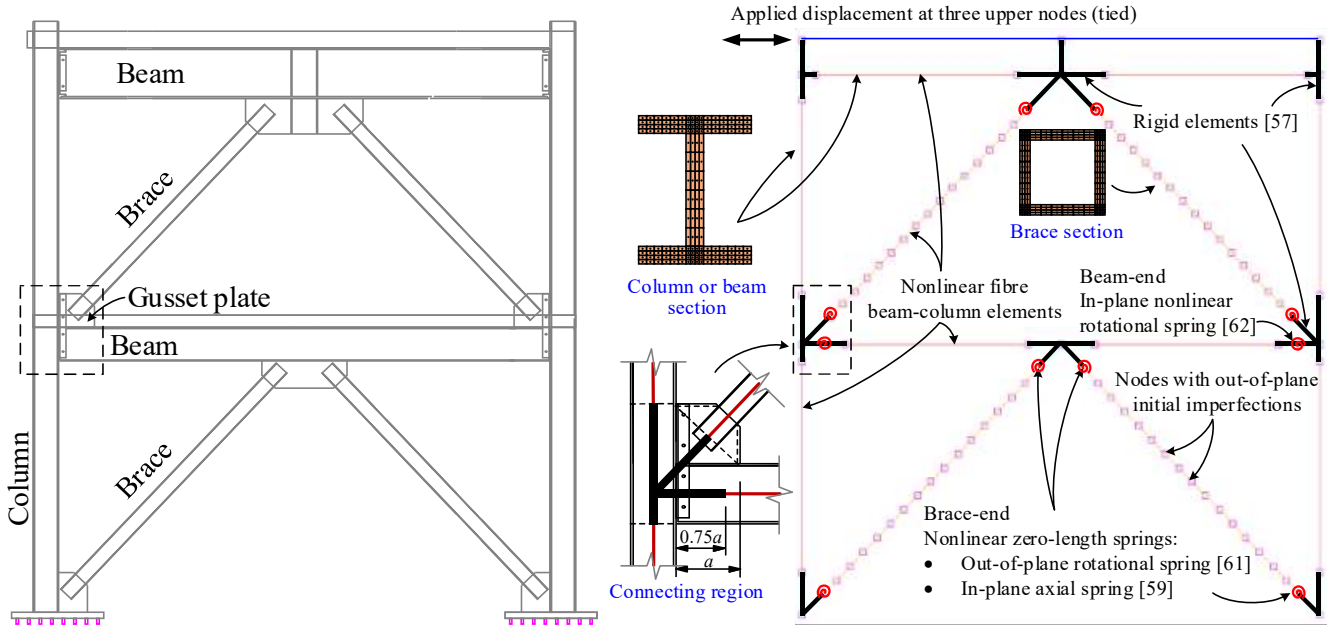
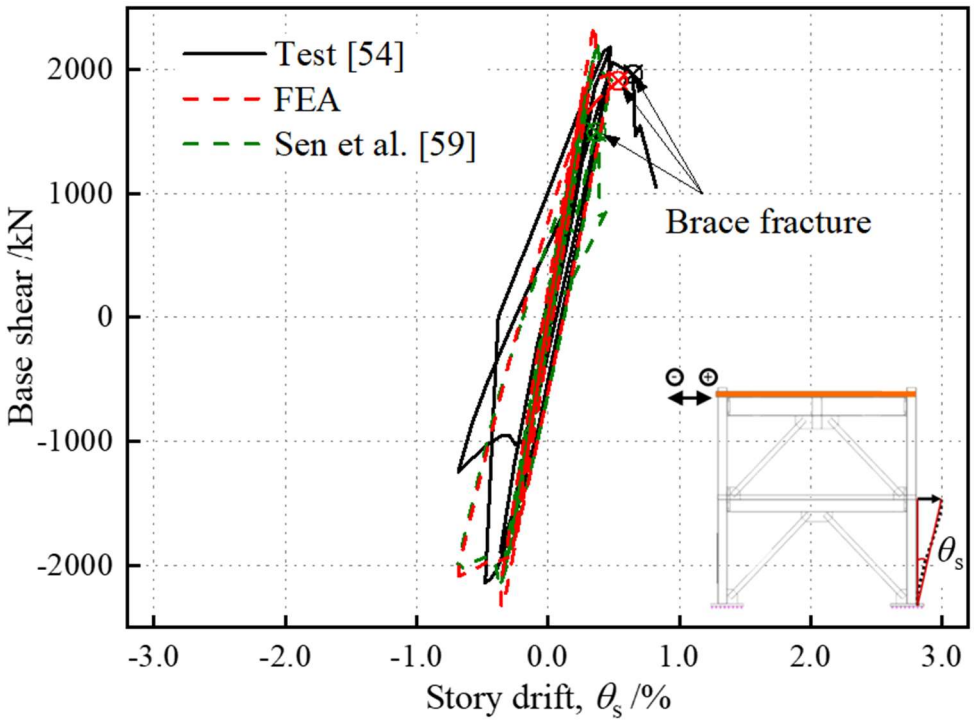


Fig. 14 Comparison between calculated and FE values of θ_G

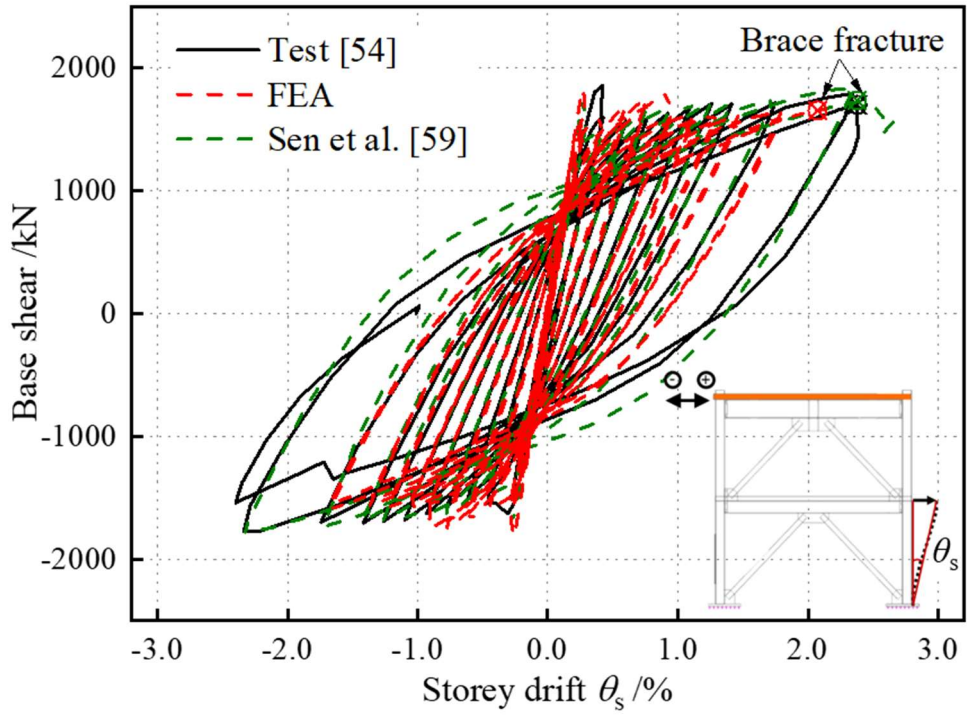


(a) Test specimen (b) Fibre-based FE model

Fig. 15. Fibre-based FE model of two-storey braced frame in OpenSees

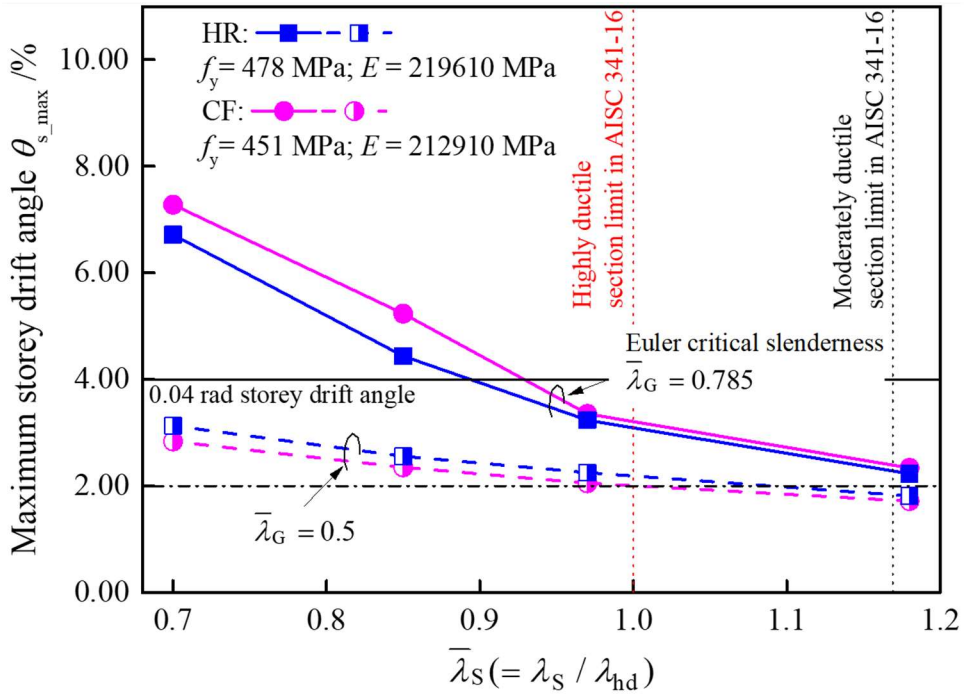


(a) TNCBF1-N-HSS

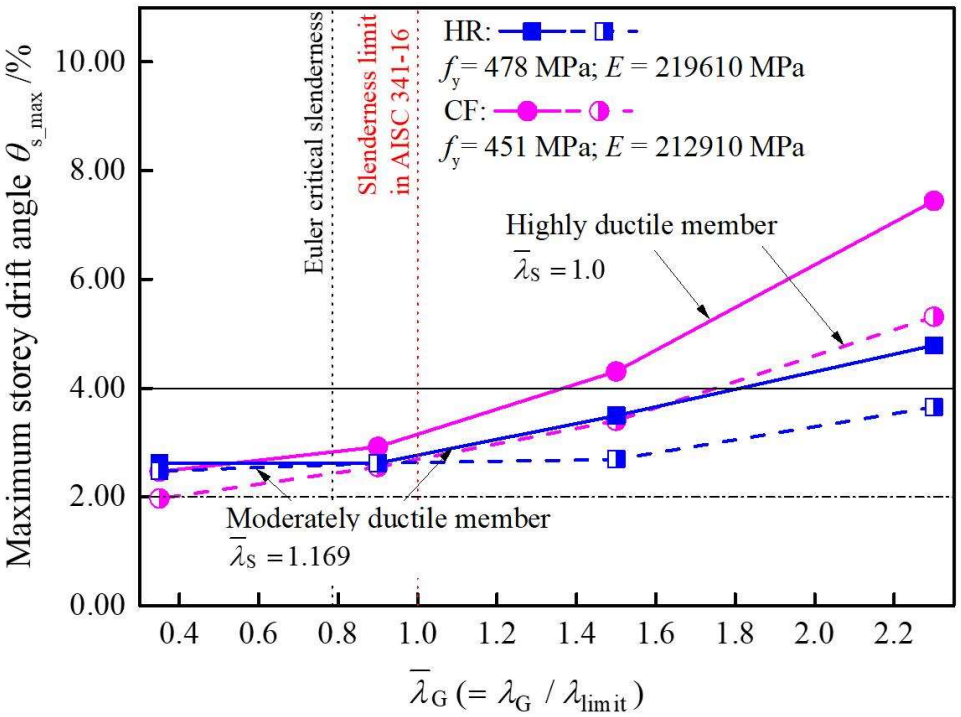


(b) TNCBF1-R-HSS

Fig. 16. Comparison of experimental and numerical responses of base shear-storey drift relationship [54, 59]



(a) Effect of $\overline{\lambda}_S$; $\overline{\lambda}_G = \dfrac{KL/r}{\lambda_{limit}}$



(b) Effect of $\overline{\lambda}_G$; $\overline{\lambda}_S = \dfrac{B'/t}{\lambda_{hd}}$

Fig. 17 Maximum storey drift angle before brace fracture

Table 1. Summary of nominal dimensions and measured material properties of brace specimens

Brace type and shape/loading protocol	Label	B (r_s) (mm)	t (mm)	B'/t	L (mm)	$\lambda_G = KL/r$	E (GPa)	f_y (MPa)	f_u (MPa)
SHS tube/ Type A [2]	40×40×3×1250-CS-CF	40.0 (3.00)	3.0	9.3	1250	41	212.9	451	502
	40×40×3×2050-CS-CF	40.0 (3.00)	3.0	9.3	2050	68	212.9	451	502
	40×40×4×2050-CS-CF	40.0 (3.50)	4.0	6.25	2050	69	201.6	410	430
	60×60×3×2050-CS-CF	60.0 (4.00)	3.0	15.3	2050	44	207.4	361	402
	40×40×3×1250-CS-HR	40.0 (1.75)	3.0	10.2	1250	41	219.6	478	555
	40×40×3×2050-CS-HR	40.0 (1.75)	3.0	10.2	2050	68	219.6	478	555
	60×60×3×2050-CS-HR	60.0 (2.75)	3.0	16.2	2050	44	215.2	458	555
SHS tube/ Types B and C [3]	HSS1-1	101.6 (9.48)	6.4	10.9	2985	77	204.0	460	488
	HSS1-2	101.6 (9.48)	6.4	10.9	2985	77	204.0	460	488
	HSS2-1	101.6 (10.82)	9.0	6.9	2985	80	204.0	499	542

Notes:

CF: cold-formed steel tube; HR: hot-rolled steel tube; B: width of SHS tube; t: tube-wall thickness; r_s: internal corner radius; B': B-2(t+r_s), defined in Fig. 1; L: brace length; K: effective length factor; r: radius of gyration.

Table 2. Comparison between test and FE results

Brace type and shape/loading protocol	Label	Imperfection used in FE models		N_{GB}		N_{LB}		N_{FI}		N_{CO}		N_{CF}	
		Global	Local	Test	FEA	Test	FEA	Test	FEA	Test	FEA	Test	FEA
SHS tube/ Type A [2]	40×40×3×1250 -CS-CF	*L*/1500	*t*/150	4	3	8	8	--	10	10	NO	11	NO
	40×40×3×2050 -CS-CF*	*L*/2000	*t*/150	3	3	5	7	--	8*	10	--	11*	11*
	40×40×4×2050 -CS-CF*	*L*/2000	*t*/150	4	3	--	11	--	9*	11	--	14*	NO
	60×60×3×2050 -CS-CF	*L*/2000	*t*/150	5	4	7	7	--	8	10	8	11	NO
	40×40×3×1250 -CS-HR	*L*/1500	*t*/200	5	4	8	8	--	10	11	11	15	11
	40×40×3×2050 -CS-HR	*L*/2000	*t*/200	4	5	15	9	--	12	18	14	20	14
	60×60×3×2050 -CS-HR	*L*/2000	*t*/200	5	4	7	7	--	8	10	9	11	NO
SHS tube/ Types B and C [3]	HSS1-1-FF 101.6×6.4	*L*/1000	*t*/150	23	23	26	26	28	28	--	28	28	29
	HSS1-2-NF 101.6×6.4	*L*/1000	*t*/150	7	7	7	7	28	28	--	31	32	32
	HSS2-1-FF 101.6×9.5	*L*/1000	*t*/150	23	22	31	30	34	32	--	32	34	33

Notes:

CF: cold-formed steel tube; HR: hot-rolled steel tube; FF: far-field; NF: near-field; N_{GB}: number of cycles to global buckling; N_{LB}: number of cycles to local buckling; N_{FI}: number of cycles to fracture initiation; N_{CO}: number of cycles to corner opening; N_{CF}: number of cycles to complete fracture; t: tube-wall thickness; L: brace length.

*: Specimens failed at end connections.

--: not reported/observed in tests or did not occur in FEA (Finite Element Analysis).

NO: Not obtained due to convergence problems.

Table 3. Parameters for material model used in FE simulations

Type		$B\times t$ mm×mm	E MPa	f_y MPa	$\sigma\|_0$ MPa	Q_∞ MPa	b	C_k MPa	γ_k
Ref. [2]	HR[1]	60×3	215150	458	463	41.3	3.37	22670	109.8
		40×3	219610	478	463	40.5	4.92	7939	54.0
	CF-Flat[2]	60×3	207430	361	240	--	--	3414	21.3
								37413	552.7
		40×4	201640	410	319	--	--	5105	36.2
								53163	980.1
		40×3	212910	451	230	--	--	7910	43.3
								874954	6149.8
	CF-Corner[2]	60×3	200350	442	243	--	--	33930	156.2
								426507	3925.7
		40×4	210830	479	328	--	--	4402	30.6
								250688	2475.0
		40×3	196680	533	245	--	--	15612	59.9
								1256870	7051.7
Ref. [3]	CF-Flat	101.6×6.4	204000	460	469	69.0	6.00	2068	25.0
		101.6×9.5	204000	499	441	127.6	6.00	9997	70.0
	CF-Corner	101.6×6.4	204000	508	503	99.97	5.25	5861	160.00
		101.6×9.5	204000	502	441	127.6	6.00	9997	70.0
Parametric study	HR[1]		219610	478	463	40.5	4.92	7939	54.0
	CF-Flat		212910	451	230	--	--	7910	43.3
								874954	6149.8
	CF-Corner		196680	533	245	--	--	15612	59.9
								1256870	7051.7

Notes:

1: Values (average) from cyclic coupon tests in Ref. [50];

2: Calibrated from tensile coupon tests.

Table 4. Parameters of fracture criterion and damage evolution rule used in FE models

Type		$B\times t$ mm×mm	A MPa	n	c_1	c_2 MPa	c_g	c_h	β_1	β_2	k_h
Ref. [2]	HR	60×3	709	0.093	0.12	416.3	-6	5.5	2	2	0.6
		40×3	648	0.056	0.12	416.3	-6	5.5	2	2	0.6
	CF-Flat	60×3	502	0.058	0.12	301.5	-6	5.5	2	2	0.6
		40×4	604	0.092	0.12	322.5	-6	5.5	2	2	0.6
		40×3	568	0.054	0.12	376.5	-6	5.5	2	2	0.6
	CF-Corner	60×3	626	0.060	0.12	351.5	-6	5.5	2	2	0.6
		40×4	675	0.098	0.12	380.2	-6	5.5	2	2	0.6
		40×3	722	0.056	0.12	441.7	-6	5.5	2	2	0.6
Ref. [3]	CF-Flat	101.6×6.4	562	0.032	0.12	366.0	-6	5.5	2	2	0.6
		101.6×9.5	617	0.030	0.12	406.5	-6	5.5	2	2	0.6
	CF-Corner	101.6×6.4	615	0.027	0.12	411.8	-6	5.5	2	2	0.6
		101.6×9.5	625	0.033	0.12	406.0	-6	5.5	2	2	0.6
Parametric study	HR		648	0.056	0.12	416.3	-6	5.5	2	2	0.6
	CF-Flat		568	0.054	0.12	376.5	-6	5.5	2	2	0.6
	CF-Corner		722	0.056	0.12	441.7	-6	5.5	2	2	0.6

Table 5. Simulation matrix in parametric studies

Group	B mm	t mm	Cross-sectional slenderness $\overline{B}/t$	Member slenderness KL/r, $K = 0.5$
HR	40	2.00, 2.35, 2.70, 3.40, 4.00	16.6, 13.6, 11.4, 8.4, 6.6	34.4, 50.0, 78.4, 85.6, 114.6
	60	3.00, 3.53, 4.05, 5.10, 6.00	16.6, 13.6, 11.4, 8.4, 6.6	34.4, 50.0, 78.4, 85.6, 114.6
	80	4.00, 4.70, 5.40, 6.80, 8.00	16.6, 13.6, 11.4, 8.4, 6.6	34.4, 50.0, 78.4, 85.6, 114.6
CF	40	2.00, 2.35, 2.70, 3.40, 4.00	16.6, 13.6, 11.4, 8.4, 6.6	34.4, 50.0, 78.4, 85.6, 114.6
	60	3.00, 3.53, 4.05, 5.10, 6.00	16.6, 13.6, 11.4, 8.4, 6.6	34.4, 50.0, 78.4, 85.6, 114.6
	80	4.00, 4.70, 5.40, 6.80, 8.00	16.6, 13.6, 11.4, 8.4, 6.6	34.4, 50.0, 78.4, 85.6, 114.6

Notes:

$\overline{B} = B\text{-}2\times1.7t$

Table 6. Parameters of proposed brace fracture initiation models

Group	θ_G		
	A_θ	B_θ	C_θ
HR	0.227	-0.789	0.392
CF	0.238	-0.806	0.553

Table 7. Cross-sections and material properties of CBF members [54]

Member	Cross-section details $h \times b_f \times t_w \times t_f$ or $B \times t$ (mm)	Yield strength (MPa)	Tensile strength (MPa)
Column	W12×72 312×305×10.9×17.0	395	506
First floor beam	W16×45 409×179×8.76×14.4	414	521
Second floor beam	W24×94 617×230×13.1×22.2	460	535
Braces for TNCBF1-N-HSS	SHS7×7×1/4 178×6.35	443	508
First-storey braces of TNCBF1-R-HSS	SHS5×5×3/8 127×9.53	438	504

Notes:

W: wide-flange I-shape section; SHS: square hollow section; h: cross-sectional height of I-shape section; b_f: flange width of I-shape section; t_w: web thickness of I-shape section; t_f: flange thickness of I-shape section; B: width of SHS tube; t: tube-wall thickness.